Brodogradnja Volume 77 Number 4 (2026) 77415

University of Zagreb Faculty of Mechanical Engineering and Naval Architecture

journal homepage: www.brodogradnja.fsb.hr

Brodogradnja

An International Journal of Naval Architecture and Ocean Engineering for Research and Development

Numerical investigation on EGR strategy and combustion-emission characteristics for a large two-stroke marine ammonia/diesel dual-fuel engine across the entire operating envelope

Xianfu Ma[1], *Daoyi Lu*[1,*], *Juntian Liu*[1], *Huaiyu Wang*[2], *Keying Cui*[3], *Huibing Gan*[1]

[1]*Marine Engineering College, Dalian Maritime University, Dalian 116026, China*
[2]*College of Power and Energy Engineering, Harbin Engineering University, Harbin, 150001, China*
[3]*Dalian Marine Diesel Co., Ltd, Dalian 116021, China*

ARTICLE INFO

Keywords:
Ammonia/diesel engine
High-pressure direct injection
Exhaust gas recirculation
Entire operating envelope
NO_X reduction

ABSTRACT

To balance NO_X emissions and performance in ammonia-fueled marine engines, this study investigates exhaust gas recirculation (EGR) effects on combustion, performance, and emissions, and proposes a full-load EGR strategy. Based on a validated CFD model of a methanol/diesel dual-fuel engine and an ammonia spray model, an ammonia/diesel dual-fuel engine model was developed. Simulations at four typical loads were conducted with various EGR rates. Results show that higher EGR slows ammonia combustion, prolongs combustion duration, intensifies after-burning, and increases ammonia emissions. Heat release rate is load-dependent, with peaks regulated by EGR. Engine performance varies with load: the gross indicated mean effective pressure ($IMEP_g$) increases with EGR at low-to-medium loads, but first rises then decreases at high loads. EGR effectively reduces NO_X emissions at all loads, with maximum reduction ranging from 71.5 % to 90.2 %. Fuel NO_X shows higher sensitivity to EGR than thermal NO_X. However, EGR also increases ammonia and N_2O emissions—marginal at low loads but significant at medium-to-high loads, with a distinct surge threshold. Recommended EGR rates are 50 %, 40 %, 30 %, and 10 % at 25 %, 50 %, 75 %, and 100 % loads, respectively. This strategy enables compliance with IMO Tier III NO_X regulations, achieves low ammonia and N_2O emissions, and improves $IMEP_g$.

1. Introduction

The shipping industry, as one of the most important transportation modes in international trade, undertakes over 80 % of the global trade volume, while simultaneously generating massive greenhouse gas (GHG) emissions [1]. To mitigate the impact of shipping on the greenhouse effect, the International Maritime Organization (IMO) has proposed the 2050 carbon neutrality strategic goal [2]. Under this context, exploring the application of low/zero-carbon fuels in marine engines has become an effective pathway to reduce GHG emissions [3, 4].

* Corresponding author.
E-mail address: ludaoyi@dlmu.edu.cn

https://doi.org/10.21278/brod77415
Received 25 February 2026; Received in revised form 10 August 2026; Accepted 11 August 2026
Available online 04 September 2026
ISSN 0007-215X; eISSN 1845-5859

Hydrogen and ammonia, as representative zero-carbon fuels [5, 6], exhibit tremendous application potential in the field of transportation. Neither fuel contains carbon atoms in its molecular structure, a characteristic that determines hydrogen and ammonia do not generate CO_2 during combustion. Compared with hydrogen, ammonia possesses three prominent advantages [7]: (1) ammonia possesses higher volumetric energy density to ensure providing more energy under the same storage space; (2) under normal temperature conditions, ammonia only requires -33°C to liquefy, which is more economical and practical compared to the liquefaction condition of -253°C for hydrogen; (3) more than 120 ports globally already meet ammonia loading and unloading conditions, with established storage and transportation infrastructure. Therefore, selecting ammonia as an alternative fuel for marine diesel has become a more practically feasible and ideal carbon reduction pathway.

Although ammonia is regarded as a highly potential alternative fuel for marine engines, it possesses inherent characteristics of difficult ignition and low flame propagation speed [8], leading to the fact that a single ammonia fuel engine is difficult to meet the engineering requirements of combustion stability and power output for marine power. Therefore, the dual-fuel combustion mode of "diesel ignition - ammonia main combustion" has become a more feasible technical pathway to balance the cleanliness of ammonia fuel and engine practicality [9]. Current research in this field mainly focuses on two technical modes: low-pressure ammonia gas injection premixed combustion (LPGI) and high-pressure liquid ammonia direct injection combustion (HPDI) [10].

For the LPGI mode, Reiter et al. [11] realized operation with an ammonia energy ratio as high as 95 % on an ammonia/diesel dual-fuel (ADDF) engine using port injection, verifying the technical feasibility of high ammonia substitution rates. Zhu et al. [12] conducted numerical simulations of combustion characteristics of low-pressure ammonia gas injection based on a computational fluid dynamics (CFD) simulation model of a two-stroke natural gas/diesel marine engine. The results indicated that compared to the pure diesel combustion mode, the addition of ammonia within a suitable ammonia energy ratio range can improve the in-cylinder combustion process, thereby enhancing engine combustion efficiency. Nevertheless, the study by Liu et al. [13] also pointed out significant defects of the LPGI mode, namely the tendency to produce substantial unburned ammonia slip and N_2O emissions.

Regarding the HPDI mode, relevant studies have demonstrated greater potential for synergy between performance and emissions. Zhou et al. [10] compared the combustion and emissions characteristics of the LPGI mode and the HPDI mode. The results showed that the indicated thermal efficiency (ITE) of the engine in both modes could reach over 50 %, while the emissions of the HPDI mode under appropriate conditions were significantly lower than those of the port premixed mode. Zhang et al. [14] carried out an experimental study on the ammonia/diesel dual direct injection strategy on a small-scale single-cylinder low-compression-ratio two-stroke engine. The results indicated that the direct-injected high-energy diesel spray can enhance the ignition and combustion process of ammonia through a local high-temperature and high-pressure environment, effectively improving the issue of slow ammonia combustion, thereby increasing engine thermal efficiency. Simultaneously, the direct injection of liquid ammonia can promote the secondary atomization and uniform mixing of diesel spray, reducing soot emissions caused by local rich diesel combustion, and simultaneously reducing CO emissions generated by incomplete combustion.

Physical tests serve as a crucial research method for the above two combustion modes, yet they inherently suffer from high costs and potential safety hazards. In contrast, 3D-CFD simulation can acquire multi-dimensional physical field data at low cost, and has become an indispensable tool for investigating in-cylinder combustion in internal combustion engines. In the field of dual-fuel engines, Liu et al. [15] adopted CFD models to reveal the synergistic effects of EGR, hydrogen addition and pilot fuel injection timing on natural gas/diesel dual-fuel engines. Xiong et al. [16] established engine models via 3D-CFD software and clarified the coupling effects and internal mechanisms of injector layout, ammonia injection timing and energy fraction in ADDF engines. Moreover, CFD technology also facilitates research on dual-fuel schemes involving methanol, hydrogen and ammonia. Chen et al. [17] illustrated the influences of boundary parameters such as initial temperature, initial pressure and horizontal/vertical injection angles on large-scale diesel/methanol dual-fuel engines. Ma et al. [18] proposed the innovative ammonia-hydrogen coaxial stratified injection method to explore its effects on engine combustion and emission performance.

It should be noted that although ADDF engines have significant advantages in CO_2 reduction, they also face the challenge of increased emissions of pollutants such as NO_X, NH_3, and N_2O [19, 20]. Due to the nitrogen-containing characteristic of the ammonia molecular structure, its combustion process generates additional fuel NO_X [21], which is different from the mechanism where conventional diesel engines only generate thermal NO_X (formed by the reaction of N_2 and O_2 at high temperatures). The superposition of fuel NO_X and thermal NO_X easily leads to an increase in total NO_X emissions from ADDF engines. The application of ammonia fuel is expanding steadily in the marine power field. Nevertheless, whether its NO_X emissions can comply with IMO Tier Ⅲ emission standards has become an urgent core challenge, which directly restricts the marine popularization of ammonia fuel.

Among engine NO_X emission reduction technologies, the exhaust gas recirculation (EGR) technology is recognized as one of the most effective technical means for reducing NO_X emissions in traditional diesel engines [22, 23], as it regulates the combustion process through a triple mechanism of the thermodynamic inhibition (reducing peak in-cylinder combustion temperature), the chemical reaction influence (inhibiting NO_X formation reaction paths), and the oxygen dilution (reducing in-cylinder oxygen concentration). The study by Abd-Alla et al. [24] confirmed that under pure diesel combustion mode, EGR can significantly reduce engine NO_X emissions, with a 50 % reduction in NO_X at a 20 % EGR rate. Regarding the ADDF combustion, Sun et al. [25] also conducted a study on the applicability of EGR technology. The results showed that EGR also has an excellent inhibitory effect on NO_X in ADDF engines. Under the 70 % ammonia energy ratio condition, an EGR rate of only 30 % is needed to achieve a 67.87 % reduction in NO emissions, and this reduction efficiency is higher than that under pure diesel mode with the same EGR rate, verifying the application potential of EGR technology on ADDF engine models.

Although the NO_X reduction effect of EGR technology on ADDF engines has been preliminarily verified, the following technical gaps still exist in current research: (1) the application research of EGR technology on ADDF engines mainly focuses on the LPGI mode, while studies on the EGR adaptability for the HPDI mode, which has better performance advantages, are rarely reported; (2) the existing studies mostly focus on a specific load condition, and there are no published literature reports on the effect of EGR on the combustion and emission characteristics of marine two-stroke ADDF engine under full-load conditions. Based on this, this study constructs a three-dimensional (3D) CFD simulation model of a two-stroke ADDF engine and selects four common loads of 25 %, 50 %, 75 % and 100 % within the full operating range. By analyzing engine changes under these loads, we can fully grasp the impacts of EGR strategies on combustion, performance and emissions under HPDI mode, and subsequently proposes a recommended EGR rate scheme compliant with IMO Tier III NO_X emissions. This research can provide theoretical support for the NO_X compliance and efficient operation of two-stroke ADDF marine engines.

The novelty of this study stems from: (1) based on the experimentally validated dual-fuel liquid injection concept, a 3D CFD simulation model of a large two-stroke high-compression ratio ADDF marine engine is constructed for the first time; (2) the combustion, performance, and emission (NO_X, NH_3, N_2O) characteristics of the engine in the low, medium, and high load ranges under wide-range EGR rate conditions are revealed; (3) the difference in sensitivity of fuel and thermal NO_X to EGR is clarified; (4) addressing the balance between NO_X emissions compliance and performance of the engine, an EGR optimization strategy oriented towards the entire operating envelope is proposed.

2. Engine modelling description

2.1 Modeling strategy

A large two-stroke HPDI dual-fuel engine, which is already in commercial operation and utilizes a main fuel with physicochemical properties relatively close to ammonia, was selected as the prototype engine. Through simulation modeling, this engine was transformed into a two-stroke ADDF engine. The modeling process is illustrated in Figure 1. First, based on the structural parameters of the prototype engine, the engine

3D geometric model was constructed using SolidWorks software. On this basis, a CFD model of the prototype engine was developed employing CONVERGE software, and the model was calibrated and validated using the control parameters and test data of the prototype engine. Next, an ammonia constant volume bomb simulation model was constructed using experimental data published by Li et al. [26] from an ammonia constant volume bomb, and the calibrated ammonia spray model was validated against this experimental data. Furthermore, the ammonia spray model was coupled with the prototype engine CFD model to establish the complete simulation model of the two-stroke ADDF engine. Finally, based on the two-dimensional (2D) and 3D results obtained from the simulation experiments, EGR's impact on the combustion characteristics, engine performance, and emission behaviors of the engine were investigated.

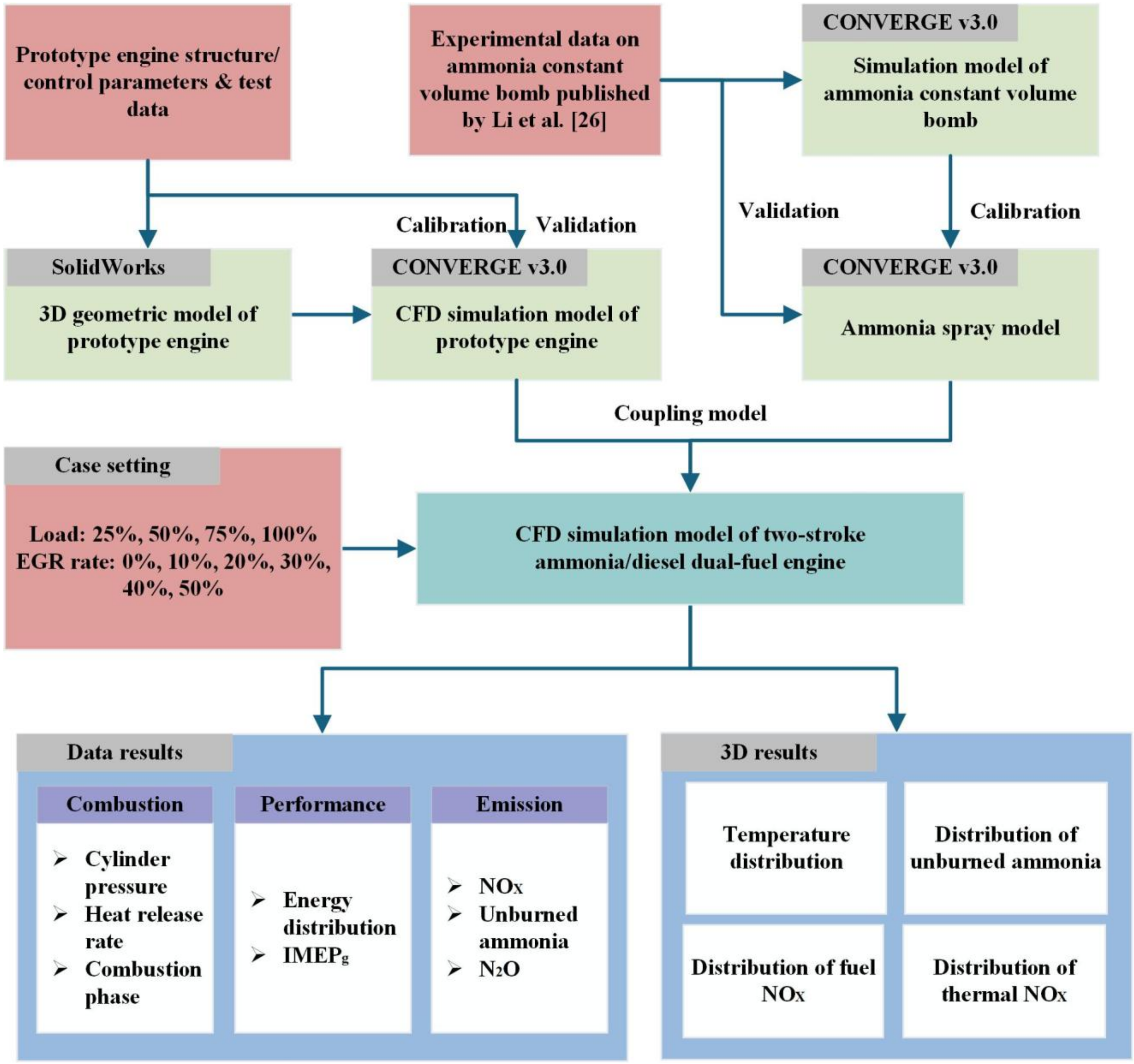

Fig. 1 Construction process of engine simulation model

2.2 Prototype engine selection

This study selected the Everllence 6G50ME-LGIM two-stroke methanol/diesel marine engine as the prototype engine [27], and its technical specifications and experimental boundary conditions are shown in Tables 1 and 2. This engine is equipped with a high-pressure common rail injection system. Two diesel injectors and two methanol injectors are arranged on the cylinder head. The four injectors work independently and only spray respective fuels. The layout of the injectors is presented in Figure 2. The engine adopts a high-pressure dual direct injection strategy. Under the dual-fuel combustion mode, the pilot diesel is first injected into the cylinder after top dead center, and the methanol is injected immediately thereafter. This injection strategy determines that the fuel combustion is dominated by diffusion combustion, enabling reliable and efficient combustion.

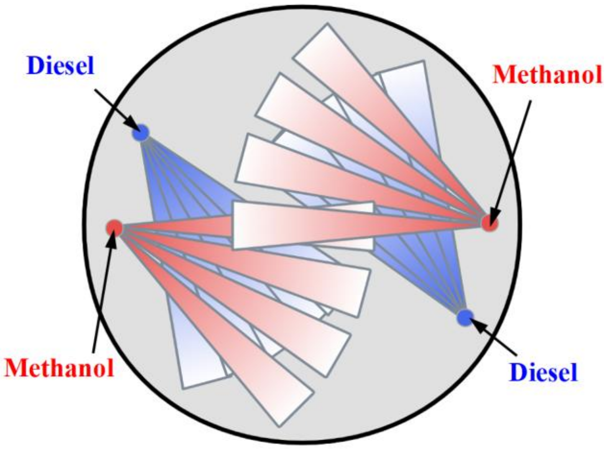

Fig. 2 Injector positions

The selection of this engine as the prototype to establish the ADDF engine simulation model was carefully considered, and the specific basis is as follows.

- Consistency of combustion logic: Ammonia features an extremely low cetane number and cannot be directly ignited via compression combustion, hence requiring high-activity fuel for pilot ignition. Accordingly, the combustion strategy of the ammonia/diesel dual-fuel engine in this study is defined as diesel pilot ignition with ammonia serving as the main fuel, consistent with that of the prototype engine.
- Reusability of core structures: The core structures of the two engine types (such as the basic power components like cylinder, piston and crankshaft) possess high reusability, eliminating the need for large-scale adjustments to the model infrastructure, significantly reducing the construction complexity of the simulation model and shortening the modeling cycle.
- Compatibility of key systems: The high-pressure common rail injection system and the diesel pilot ignition control strategy equipped on the prototype engine can be adapted to the diesel ignition requirements of the target engine without additional changes. Both methanol and ammonia maintain liquid state under normal temperature and high pressure, so the original methanol-oriented common rail hardware is applicable to ammonia supply, which reduces the model uncertainty introduced by system parameter adjustments.
- Adaptability of fuel characteristics: The lower heating values of methanol (21.2 MJ/kg) and ammonia (18.6 MJ/kg) differ by merely 12 %. Their close mass energy densities render the prototype engine's injector geometry (e.g., nozzle hole diameter, injection pressure) and injection scheduling (e.g., injection timing, fuel metering) well compatible with ammonia. Although ammonia's boiling point (239.8 K) is much lower than methanol's (337.8 K), discrepancies in spray breakup behaviors under high-pressure injection can be compensated by calibrating the KH-RT spray breakup model. Overall, the prototype injection strategy is highly adaptable to ammonia fuel; only spray model parameters related to ammonia's physical properties (such as viscosity and evaporation rate) require modification to satisfy the simulation demands of the target engine.
- Reliability of modeling method: The modeling idea based on iterative optimization of mature commercial engine models can maximize the reuse of modeling methods, boundary condition settings and error correction experiences that have been verified by engineering, effectively improving the convergence and calculation accuracy of the target model, and finally obtaining an efficient and reliable high-confidence simulation model.

In summary, the selection of this prototype engine can guarantee the feasibility and accuracy of the target engine simulation model from the aspects of combustion logic, structural reuse, system compatibility and modeling efficiency, laying a foundation for the reliability of subsequent simulation analysis. It should be noted that this prototype engine selection idea referred to the prototype engine selection idea of the marine two-stroke ADDF engine currently being developed by Everllence.

Table 1 Prototype engine specifications

Parameter	Value
Number of cylinders	6
Bore (mm)	500
Stroke (mm)	2500
Connecting rod length (mm)	2500
Compression ratio	29.58
Rated load engine speed (rpm)	80.4
Rated load engine power (kW)	6400
Number of diesel/methanol injectors	2/2
Diesel nozzle number and diameter (mm)	10×1.1
Methanol nozzle number and diameter (mm)	8×1.6
Diesel/methanol injection pressure (bar)	600/430

Table 2 Boundary conditions of experimental engine

Load (%)	Parameter							
	Ambient press. (bar)	Ambient temp. (K)	Scav. press. (bar)	Scav. temp. (K)	Exhaust press. (bar)	Exhaust temp. (K)	Methanol fuel mass (g/cycle)	Diesel fuel mass (g/cycle)
25	1.02	296	1.51	301	1.42	503	25.56	3.99
50	1.02	296	1.89	297	1.77	593	42.59	3.95
75	1.02	297	2.86	301	2.8	623	55.8	3.266
100	1.02	298	3.65	308	3.62	683	72.84	2.656

2.3 Prototype engine modeling and validation

First, the 3D geometric model of the engine cylinder was developed based on the structural parameters of the prototype engine. The model is divided into two parts: the in-cylinder region and the exhaust region, wherein the in-cylinder region includes the cylinder liner, cylinder head, piston and piston rings, and the exhaust region includes the exhaust valve and exhaust port. Further, the CFD simulation model was constructed based on the CONVERGE v3.0 software, as depicted in Figure 3. Table 3 lists the primary initial and boundary conditions, and the exhaust valve lift profile is also provided in Figure 4. It should be noted that the profile has been simplified using a piecewise linear approximation, although the actual lift curve still exhibits slight rounded transitions over the limited crank angle intervals near the opening and closing phases. Given that these transition regions occupy only a very small fraction of the total exhaust valve open duration, any local perturbations introduced by this simplification are expected to have a negligible impact on the simulation outcomes. Consequently, the resulting errors are not significant enough to affect the principal conclusions of this study. The calculation process starts from the scavenging port closing time (-143.6 °CA ATDC) and continues to the scavenging port opening time (143.6 °CA ATDC). Variable time step algorithm is adopted in the research. The time step follows the recommended value of CONVERGE setting. The initial time step is set to $1 \cdot 10^{-7}$ s, and the maximum time step is limited to 0.0001 s. During intense reactions such as spray and combustion, the time step can be automatically adjusted down to a minimum of $1 \cdot 10^{-8}$ s to guarantee calculation accuracy and numerical stability.

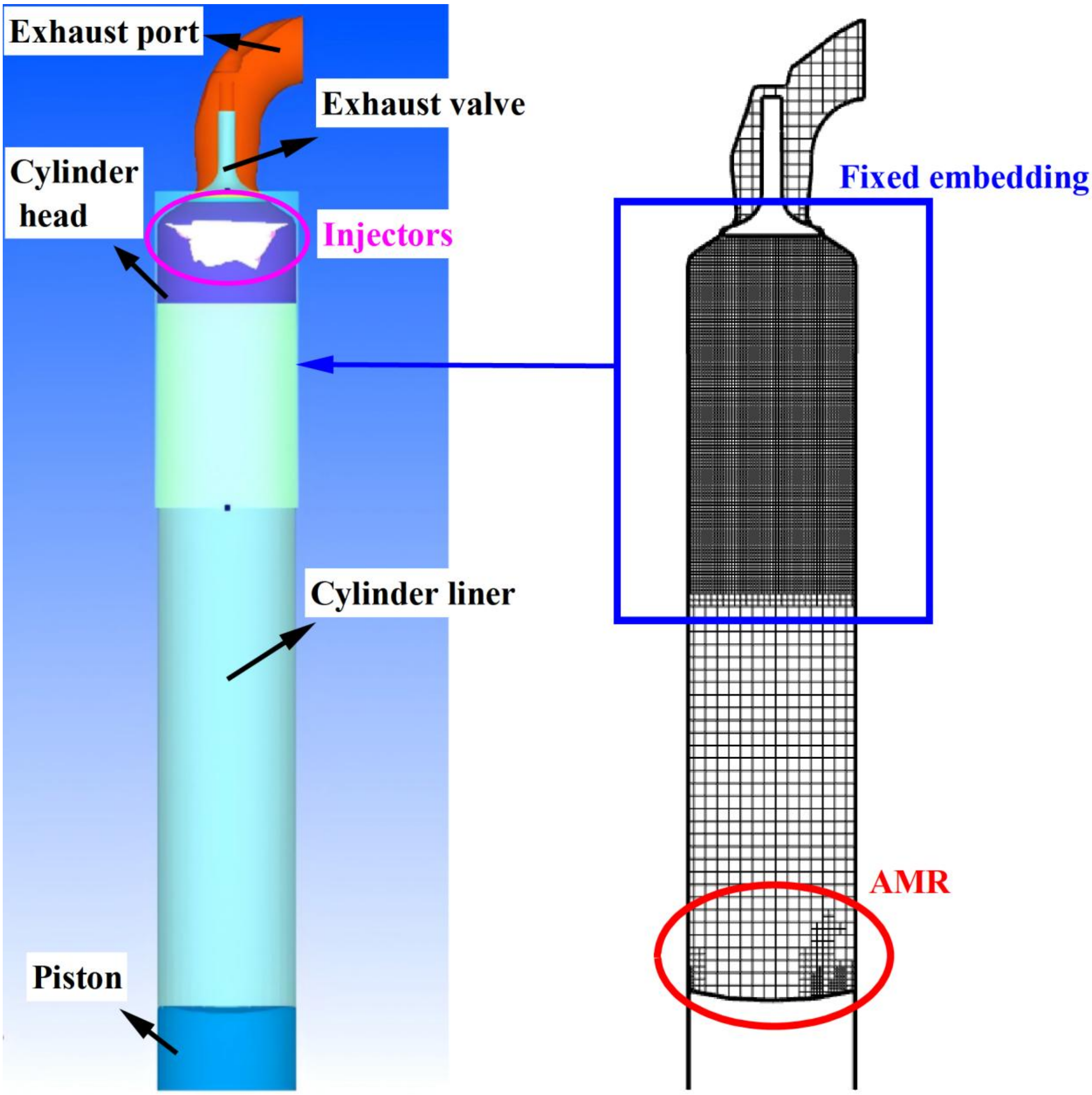

Fig. 3 Engine simulation model (left) and encryption strategy (right)

Table 3 Initial and boundary conditions of simulation model

Load (%)	Parameter				
	Initial cylinder press. (bar)	Initial cylinder temp. (K)	Piston temp. (K)	Head temp. (K)	Line temp. (K)
25	1.6	366.4	523	503	463
50	1.84	370.1	551	531	491
75	2.88	415.9	573	553	513
100	3.66	435.8	623	603	563

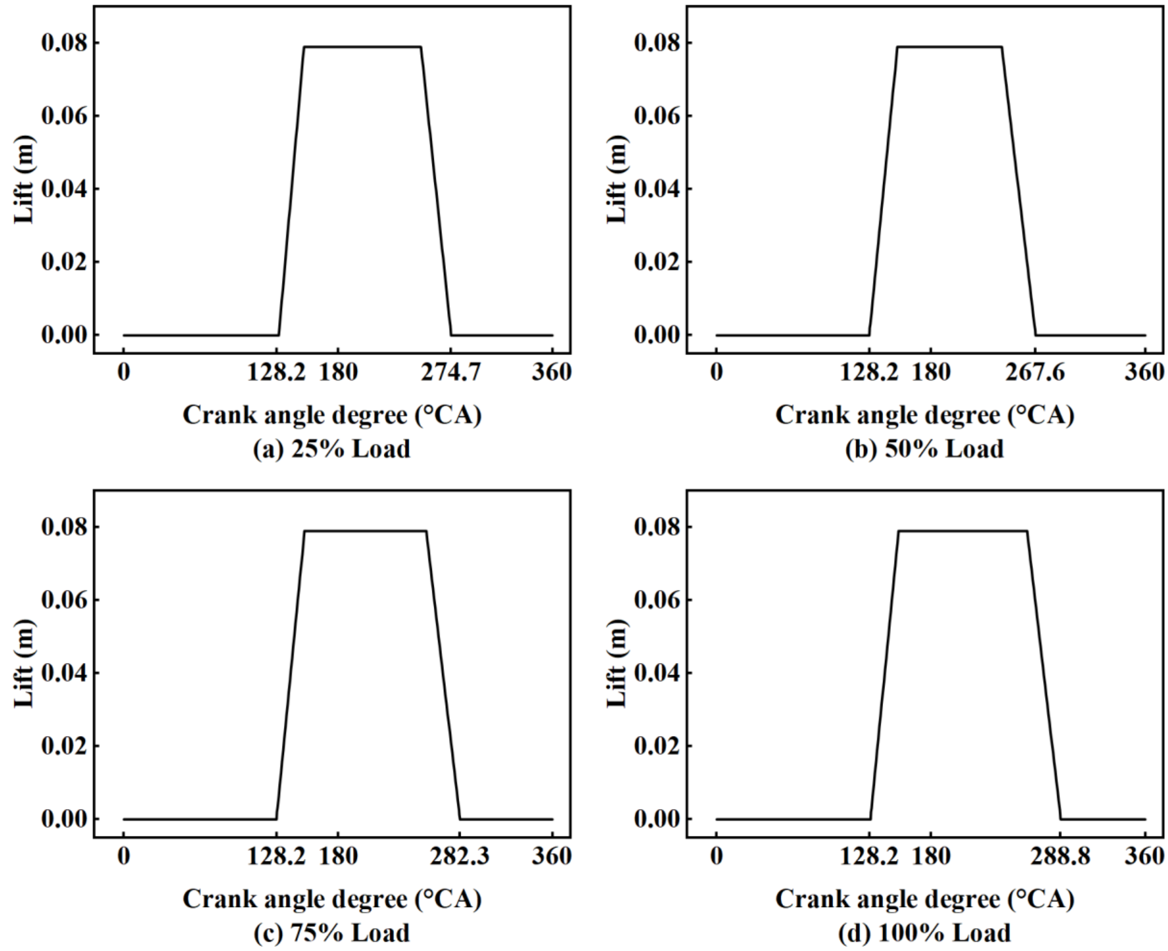

Fig. 4 Exhaust valve lift profile

To accurately simulate the in-cylinder flow and mixing combustion processes, appropriate simulation sub-models were selected, as shown in Table 4. The turbulent flow is calculated using the RNG k-ε turbulence model [28]; the fuel spray breakup process is described by the KH-RT model [29]; the liquid injection is simulated by the Blob model [30]; the droplet evaporation adopts the Frossling model [31]; the droplet collision employs the NTC model [32]; and the droplet wall impingement uses the Wall film model [33]. In addition, the SAGE combustion model based on detailed chemical kinetics is selected, and based on the similarity in combustion characteristics between diesel and n-heptane, n-heptane is chosen as a surrogate for diesel simulation. The chemical kinetic mechanism for in-cylinder combustion adopts the methanol-diesel dual-fuel chemical kinetic mechanism proposed by Liu et al. [34], which has been validated by numerous studies. The wall heat transfer employs the O'Rourke and Amsden model [35], while for emission models, the NO_X formation model adopts the Zeldovich mechanism [36], and the soot generation and oxidation model uses the Hiroyasu-NSC model [37].

Table 4 Selection of simulation sub-models

Model name	Sub-models
Turbulence	RNG *k-ε* [28]
Spray break-up model	KH-RT [29]
Liquid injection model	Blob [30]
Drop evaporation	Frossling [31]
Drop collision	NTC [32]
Spray-wall interaction model	Wall film [33]
Combustion	SAGE chemical reaction solver
Wall heat transfer	O'Rourke and Amsden [35]
NOx generation	Extended Zeldovich mechanism [36]

Since the mesh size in CONVERGE software significantly affects the simulation results, considering the characteristics of the large bore and long stroke of the engine in this study, different levels of fixed embedding and Adaptive Mesh Refinement (AMR) strategies were first adopted to improve the accuracy of the simulation results. Specifically, a level 2 fixed embedding strategy was adopted for the cylinder liner and cylinder head, a level 3 fixed embedding strategy was adopted for the exhaust valve, and a level 3 fixed embedding strategy was adopted for the diesel and methanol spray development regions. Meanwhile, a level 2 adaptive mesh refinement strategy was adopted for the in-cylinder velocity and temperature calculation mesh.

Keeping the embedding strategy unchanged, the base grid size was changed to perform grid independence validation. Since the engine bore in this study is large, an excessively small grid size tends to cause the computational feasibility to deteriorate, so this study set the base grid sizes to 30, 35, 45, and 65 mm, respectively. Figure 5 shows the influence of mesh size on the in-cylinder pressure of the engine at 25 % load. Among them, the in-cylinder pressure curve with a base grid size of 35 mm is already very close to that with a base grid size of 30 mm, while deviations appear in the corresponding in-cylinder pressure curves when the base grid size is 45 mm and above. Considering the computational accuracy and efficiency of the model, a base grid size of 35 mm was adopted for the simulation calculations.

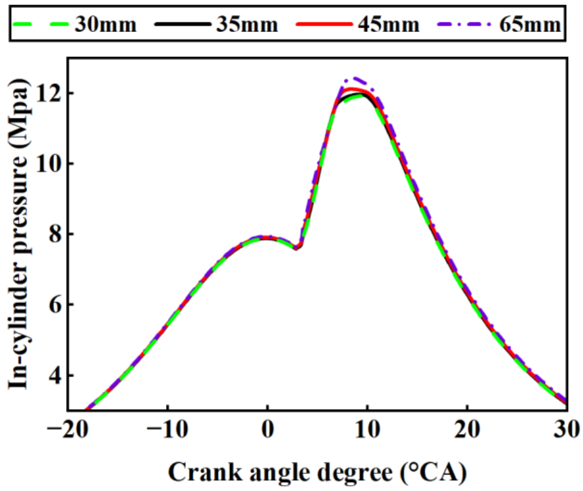

Fig. 5 Influence of the basic grid on the cylinder pressure

Based on the factory test data of the prototype engine [38], the calibration and validation of the engine CFD simulation model were performed for four loads of 25 %, 50 %, 75 %, and 100 % under the dual-fuel mode. Figures 6 and 7 show the simulation results of the in-cylinder pressure curves and key parameters under different loads. The experimental gross indicated mean effective pressure ($IMEP_g$) corresponds to the full-cycle value, whereas the simulated $IMEP_g$ excludes work generated during the scavenging phase. As observed from the measured pressure curves, that the in-cylinder pressure remains low and nearly constant throughout the scavenging phase, and the work contribution from this interval can be approximately neglected. Accordingly, excluding the scavenging-phase work from the simulated $IMEP_g$ leads to only limited deviations. For the comparison between simulated and measured cylinder pressure in Figure 7, the deviation quantification analysis shows that, under the four operating conditions, the maximum deviation of the peak in-cylinder pressure is 2.5 %, the maximum deviation of the compression pressure is 1.5 %, and the errors of other validated parameters are all below 5 %, confirming that the model accuracy meets the requirements of this study.

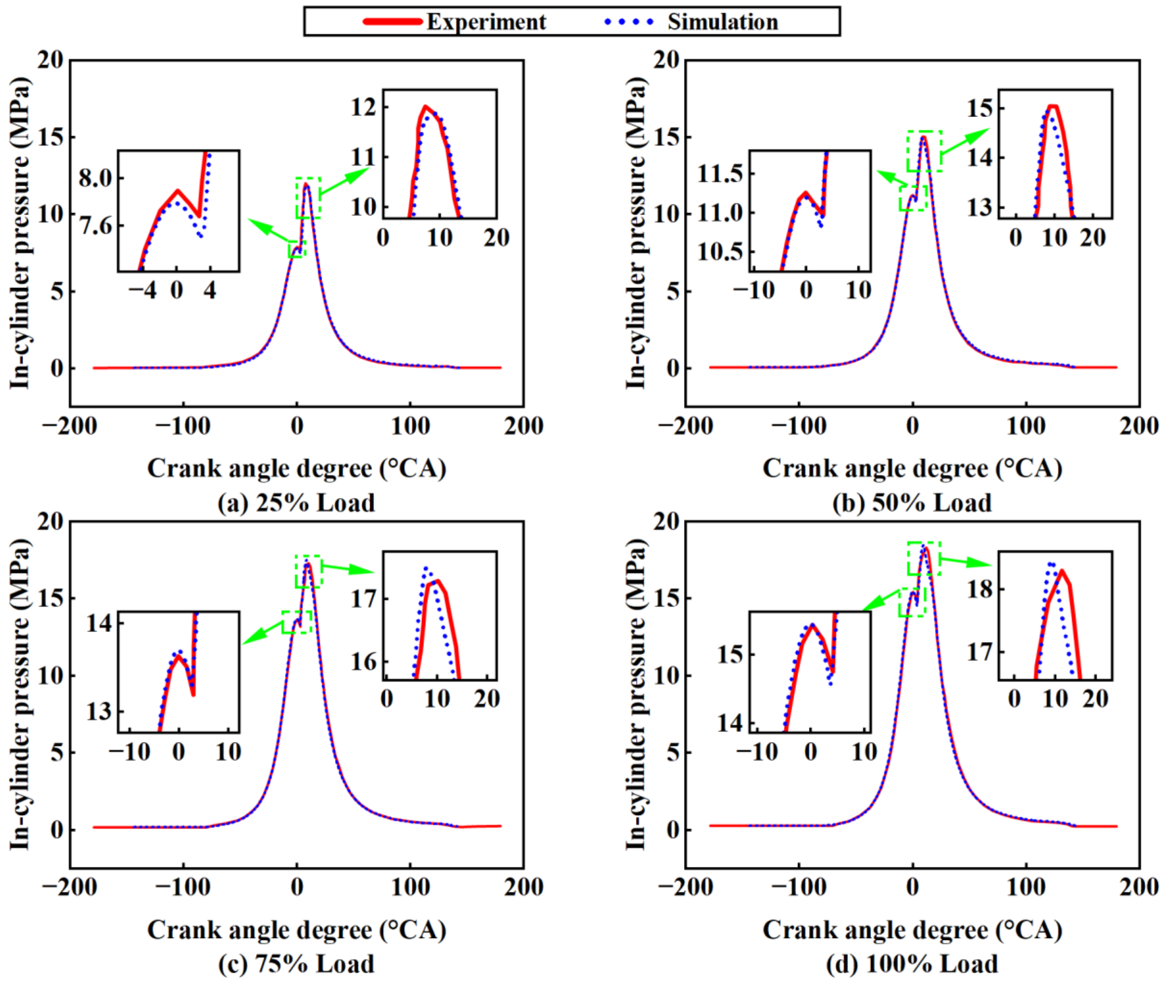

Fig. 6 Experimental vs. simulation comparison of in-cylinder pressure

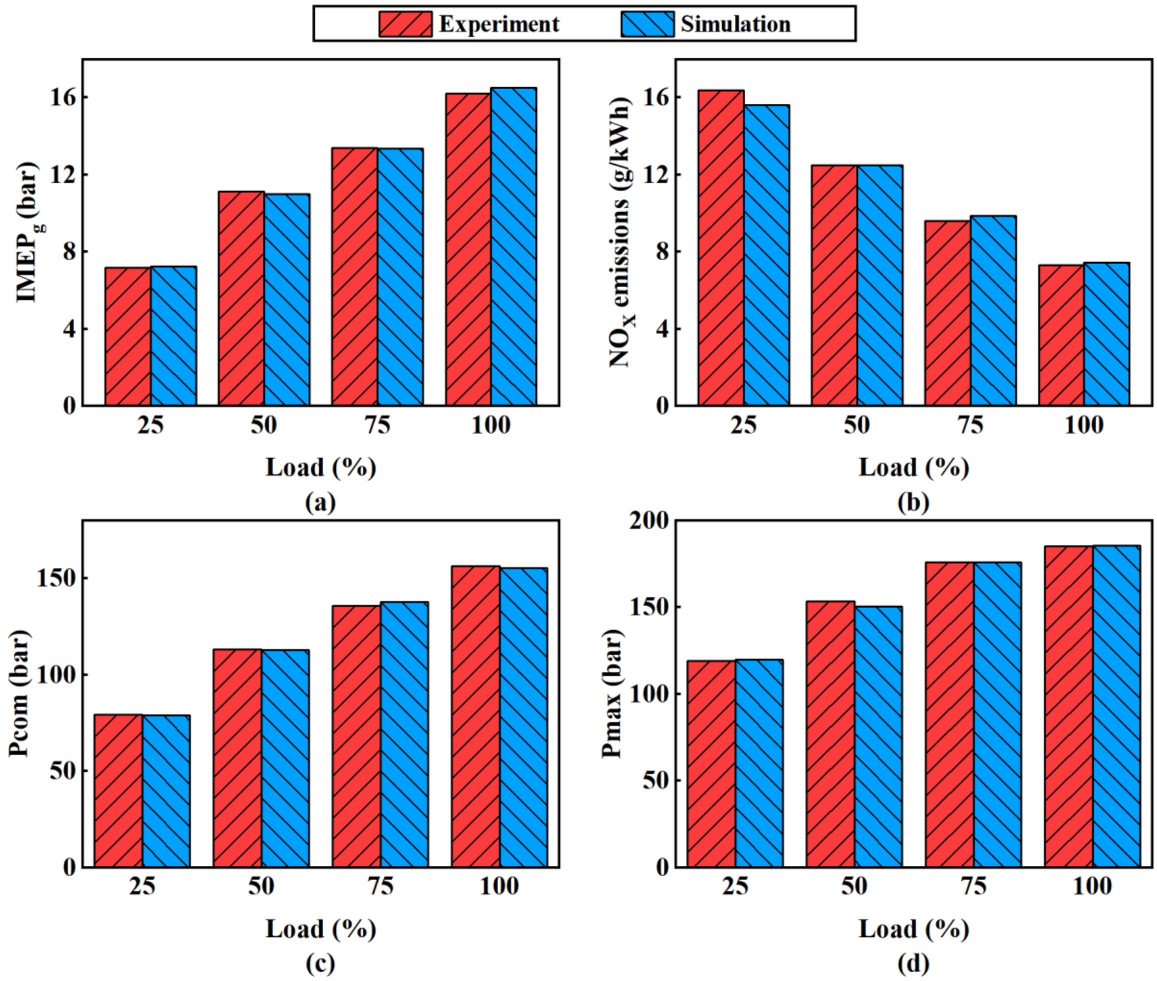

Fig. 7 Experimental vs. simulation comparison of main engine parameters

2.4 Ammonia/diesel engine modeling and validation

Accurate high-pressure liquid ammonia spray and breakup models are crucial for the combustion prediction of ammonia-diesel direct injection dual-fuel engines. The study constructed a liquid ammonia spray numerical calculation model based on the optical visualization experiments of high-pressure liquid ammonia spray and combustion processes under inert conditions conducted by Li et al. [26]. The constant volume bomb calculation domain adopted a cuboid with dimensions of 48×48×97 mm, and the boundary conditions were set according to the relevant experimental parameters, as shown in Table 5.

In order to improve accuracy and minimize calculation time, the base grid size of the model was set to 6.4 mm, and a level 2 adaptive mesh refinement strategy was selected for the velocity gradient and temperature gradient. Based on the finding by Zhou et al. [10] that the calculation results of liquid ammonia spray penetration distance show little difference when the ratio of mesh size to nozzle diameter (M/D) in the near-nozzle region is approximately 1.1-2.1, a level 4 fixed embedding strategy was selected in the spray development region. At this point, the mesh size of the ammonia spray part reaches 0.4 mm, and the M/D of the liquid ammonia constant volume bomb model is 1.82, which satisfies the simulation conditions.

Table 5 Liquid ammonia spray experimental conditions

Parameter	Value
Number of nozzles	1
Nozzle diameter (mm)	0.22
Fuel injection pressure (MPa)	60
Injection duration (ms)	2.5
Fuel temperature (K)	350
Ambient temperature (K)	900
Ambient density (kg/m^3)	18
Ambient gas	N_2

Figure 8 shows the comparison results between the experiment and simulation of liquid ammonia spray gas-liquid phase penetration distances under experimental conditions. The overall fitting effect of two-phase penetration distance is satisfactory. Minor deviation only occurs in gas-phase penetration distance at the late spray stage, with average relative error kept below 3 %. The simulation accuracy meets research requirements. Figure 9 shows the comparison between the experiment and simulation of liquid ammonia spray morphology under experimental conditions, where the solid line is the spray liquid phase contour, and the dashed line is the spray gas phase contour. It can be observed that this spray model can predict the morphological development of liquid ammonia spray well and can be used for subsequent numerical simulation research.

Based on the CFD simulation model constructed in Section 2.3, methanol was changed to ammonia fuel, and the liquid ammonia spray sub-model was set up to construct the ADDF engine CFD model. In terms of simulation settings, the liquid ammonia injection pressure was maintained at 60 MPa, and the injector orifice diameter was set to 1.6 mm. A 4-level fixed refinement was applied to the ammonia injector and spray development area; at this point, the M/D ratio in the near-nozzle region of the ammonia injector was 1.37, which ensures the accuracy of liquid ammonia spray prediction. For the chemical reaction kinetics mechanism of in-cylinder combustion, the ammonia-n-heptane combined combustion chemical reaction mechanism developed and validated by Zhou et al. [39] was adopted, which includes 65 species and 344 reactions. Based on the above model and parameter settings, further research on the EGR strategy and characteristics of the ADDF engine was carried out. It should be noted that partial model validation has been accomplished, yet sufficient experimental verification is still lacking regarding the overall performance characteristics and EGR action mechanism of ADDF engines, which may slightly raise the simulation deviation of the model.

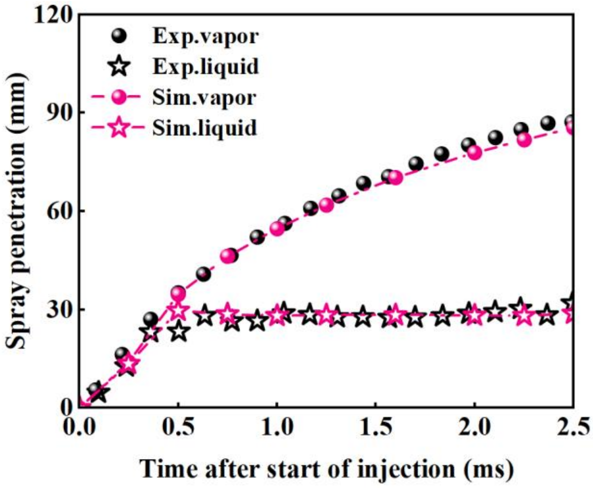

Fig. 8 Comparison of spray penetration distance of high-pressure liquid ammonia

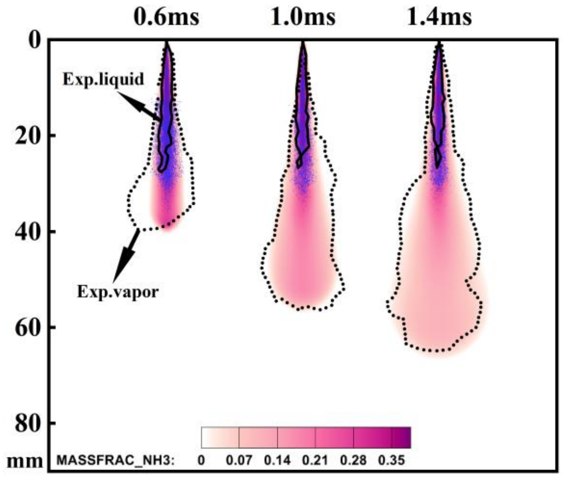

Fig. 9 Comparison of spray patterns of high-pressure liquid ammonia

3. Study Cases setting

Utilizing the developed simulation model of the ADDF engine, this paper examines the impacts of EGR on the engine's combustion behaviors, operational performance, and emission characteristics under dual-fuel mode. Simulation cases are set up for four load conditions: 25 %, 50 %, 75 %, and 100 %. Specifically, the 100 % load condition of the ADDF engine is defined based on the factory specifications of the prototype engine at 100 % load, where methanol fuel is replaced by ammonia fuel. Except for specific parameters adjusted according to fuel property differences, all other parameters remain consistent with the prototype engine's 100 % load settings. Under the 100 % load condition, the ammonia injection mass is 72.8425 g/cycle and the diesel injection mass is 2.65561 g/cycle, and these fuel injection parameters have been supplemented in Table 2. The air-fuel ratio at 0 % EGR rate under 100 % load is approximately 18.35. For each load, EGR rates of 10 %, 20 %, 30 %, 40 %, and 50 % are selected. To eliminate the interference of other factors, model parameters (including injection pressure, single-cycle injection mass, injection rate profile, and other boundary conditions for both ammonia and pilot diesel) are kept constant for different EGR rates under the same load. The corresponding ammonia energy fractions at 25 %, 50 %, 75 % and 100 % engine load are 72.6 %, 81.7 %, 87.6 % and 91.9 % respectively.

In this study, the exhaust gas components are reasonably simplified based on ammonia combustion characteristics. This method is carefully formulated with reference to the successful cases reported by Hu et al. [38]. Firstly, major ammonia combustion products including N_2 and H_2O, CO_2 generated from diesel combustion, and O_2 involved in combustion reactions are retained. Meanwhile, unburned ammonia and N_2O that supports combustion at high temperatures are incorporated to mitigate environmental pollution. Finally, other trace exhaust gases are categorized into N_2 components owing to the inert property of nitrogen. This simplification strategy maintains component concentration balance, reduces reaction computation load, and improves calculation efficiency and numerical stability. The EGR rate is defined as follows:

$$R_{EGR} = \frac{m_{EGR}}{m_{EGR} + m_{AIR}} \times 100\ \% \tag{1}$$

where m_{AIR} represents the fresh air mass entering the cylinder when the scavenging port closes, and m_{EGR} represents the exhaust gas mass recirculated into the cylinder when the scavenging port closes. The gas component settings for all study cases are shown in Table A.1.

The ITE was used to analyze the engine combustion characteristics, and its calculation formula is as follows:

$$R_{ITE} = \frac{W_{gross}}{\left(m_{NH_3,fuel} + m_{NH_3,EGR}\right) \times LHV_{NH_3} + m_{diesel} \times LHV_{diesel}} \times 100\ \% \tag{2}$$

where W_{gross} is the net indicated work done by the piston over the simulation interval (i.e., from -143.6 °CA ATDC to 143.6 °CA ATDC), which equals the expansion work minus the compression work. This parameter is obtained by integrating the in-cylinder pressure with respect to the cylinder volume change, where the compression work is taken as negative and the expansion work as positive. $m_{NH_3,fuel}$, $m_{NH_3,EGR}$, and m_{diesel} represent the masses of fuel ammonia, recirculated ammonia, and pilot diesel, respectively. LHV_{NH_3} and LHV_{diesel} represent the lower heating values of ammonia and diesel, respectively, where the LHV of ammonia is taken as 18.6 MJ/kg and the LHV of diesel is taken as 44.9 MJ/kg.

To facilitate the analysis of the effect of EGR on combustion phasing, this paper defines CA10, CA50, and CA90 as the crank angles where the cumulative in-cylinder heat release reaches 10 %, 50 %, and 90 % of the total heat release, respectively. Among them, CA50 represents the center of combustion; the crank angle interval from the start of diesel injection to CA10 is defined as the ignition delay period; and the crank angle interval from CA10 to CA90 is defined as the combustion duration.

4. Results and discussion

4.1 Analysis of engine combustion characteristics

Figures 10 and 11 illustrate the impacts of varied EGR rates on the heat release rate (HRR) and cylinder pressure of the engine at 25 %, 50 %, 75 % and 100 % loads. A distinct feature is that the compression pressure and maximum pressure of the engine decrease with the increase of the EGR rate under all loads. Since triatomic molecules in the exhaust gas, such as CO_2, H_2O, and N_2O, have higher specific heat capacities than diatomic molecules like O_2 and N_2, EGR suppresses the temperature rise of the working medium, leading to a reduction in compression pressure. The decline in peak pressure results from the combined effects of EGR. Primarily, EGR reduces in-cylinder oxygen concentration and slows down combustion. Besides, the cooling effect of high-specific-heat EGR gas and the chemical influence of water vapor on reaction pathways at high temperatures also exert notable impacts. The in-cylinder temperature distribution for the 75 % load condition with 0-50 % EGR rates is shown in Figure 12. This figure clearly demonstrates that the temperature in the combustion region under high EGR conditions is significantly lower than that under low EGR conditions. Observing the ammonia isosurface at 6 °CA ATDC, the area under high EGR conditions is larger than that under low EGR conditions, indicating slower ammonia combustion and milder temperature rise. Meanwhile, EGR gas with higher specific heat capacity cuts down combustion temperature. The superposition of these two effects leads to the shrinkage of high-temperature zones. In addition, it can be observed from Figure 11 that the peak heat release rate decreases with the increase of the EGR rate under all loads. Another observation is that the heat release rate in the late stage of combustion (the green dashed box in Figure 11) shows an opposite trend; that is, the heat release rate is higher under high EGR rate conditions in this stage, implying that the combustion of a larger amount of fuel is retarded. By quantifying the reduction in peak in-cylinder pressure with EGR, it is evident that the maximum pressure under high loads is more significantly affected by EGR. Taking the 50 % EGR rate as an example, the maximum in-cylinder pressures for the four loads under this condition are reduced by 4.2, 9, 11.6, and 14.1 bar, respectively, relative to the baseline condition.

A careful observation of Figure 11 reveals that the HRR of the two-stroke ammonia/diesel engine exhibit multiple peaks. The number of HRR peaks increases from two to four as the load increases from 25 % to 100 %, indicating that the combustion heat release pattern of the engine is load-dependent. The HRR peaks within the blue dashed box are inferred to be generated by diesel combustion. Taking the 75 % load case as an example for analysis, it can be observed from Figure 11(c) that there are two distinct minor peaks within the blue dashed box, which are attributed to the premixed combustion and diffusion combustion of diesel, respectively. In Figure 12, the white regions at 4 °CA and 6 °CA represent the iso-surfaces where the ammonia mass fraction is 0.01. It can be observed that the ammonia iso-surface is located in a low-temperature region at 4 °CA, whereas at 6 °CA, the ammonia iso-surface largely overlaps with the high-temperature region. This indicates that ammonia participates in combustion at 6 °CA but has not yet participated at 4 °CA. It is worth noting that the crank angle corresponding to the second peak within the blue dashed box in Figure 11(c) is approximately 4.2 °CA, implying that ammonia begins to participate in combustion only after this second peak.

As the load increases from 50 % to 100 %, the HRR exhibits a twin-peak morphology that becomes increasingly distinct. This is attributed to the fact that as the load increases, the increased ammonia injection mass prolongs the injection duration; consequently, the fuel cannot be completely burned during the main combustion stage, resulting in a larger proportion of fuel being burned in the second stage. With an increase in the EGR rate, the first HRR peak shows a downward trend, while the second peak exhibits a trend of initially rising and then falling. It is inferred that the decrease in in-cylinder temperature with increasing EGR rate leads to a reduction in the amount of combustible mixture burned at the first HRR peak, causing the continuous decline of the first peak. Consequently, more combustible mixture completes combustion during the second peak, leading to an initial upward trend in the second peak. However, while the EGR goes beyond a certain threshold, the formation of the combustible mixture becomes limited by temperature and oxygen concentration. The rate of ammonia diffusion combustion decreases, and the heat release peak gradually declines [40], resulting in the phenomenon where the second peak rises first and then falls.

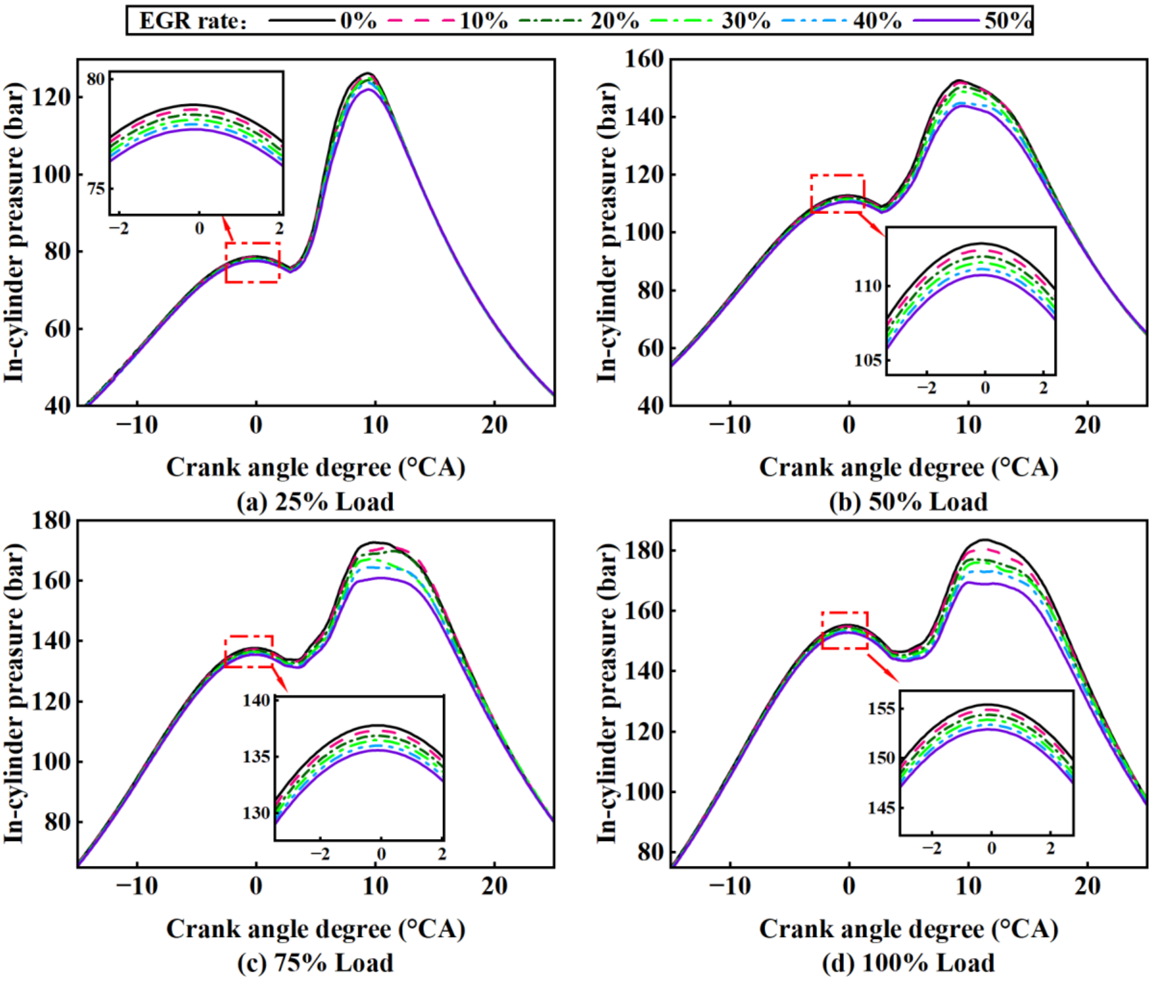

Fig. 10 Cylinder pressure under diverse loads and EGR rates

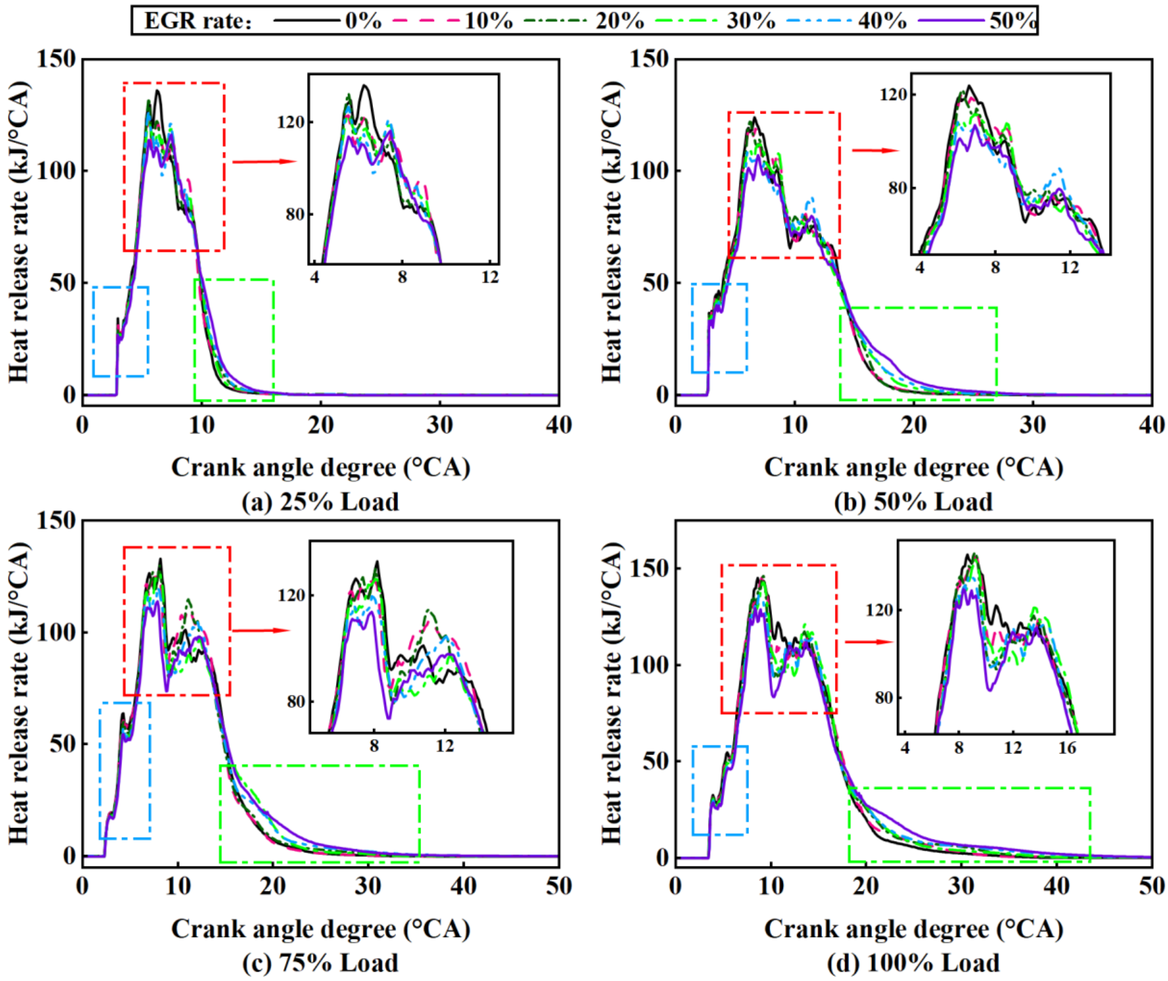

Fig. 11 Heat release rate under diverse loads and EGR rates

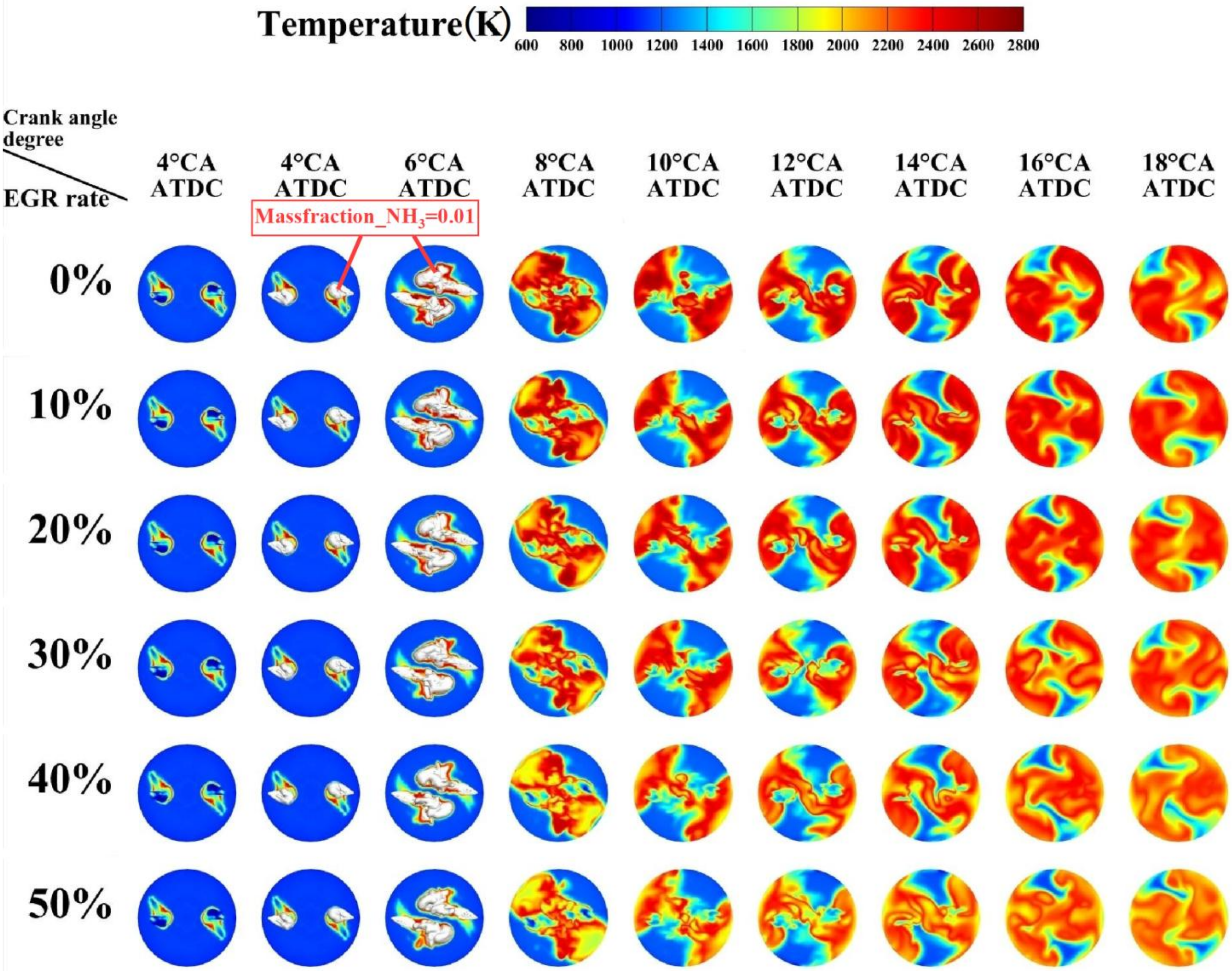

Fig. 12 In-cylinder temperature distribution under 75 % load with different EGR rates

Figure 13 presents the in-cylinder combustion duration, ignition delay and CA50 timing under various loads and EGR rates. It can be observed from Figure 13 that with the increase of the EGR rate, the ignition delay periods under all studied loads are slightly prolonged. This is because as the EGR rate increases, the in-cylinder temperature and pressure before ignition decrease (see Figure 10), thereby retarding the combustion of diesel. In general, the combustion duration exhibits an extending trend, which can be attributed to the multifaceted effects brought by EGR. Firstly, reduced oxygen concentration caused by dilution dominates the decelerated combustion. Meanwhile, EGR gas with high specific heat absorbs heat during combustion and lowers in-cylinder temperature, further slowing combustion. Additionally, exhaust gas alters reaction pathways via chemical effects. The coupling of these three effects ultimately prolongs the in-cylinder combustion duration. Taking the 50 % EGR rate as an example to compare the extension magnitude of the combustion duration across different loads, the combustion durations at 25 %, 50 %, 75 %, and 100 % loads are extended by 12 %, 17 %, 24 %, and 42 %, respectively, relative to the baseline conditions. This indicates that the combustion duration at high loads is more significantly influenced by EGR. This observation is consistent with the heat release rate curve results in Figure 11; that is, the increase in EGR rate retards the combustion rate of ammonia, causing the heat release peaks to transition from steep to flat.

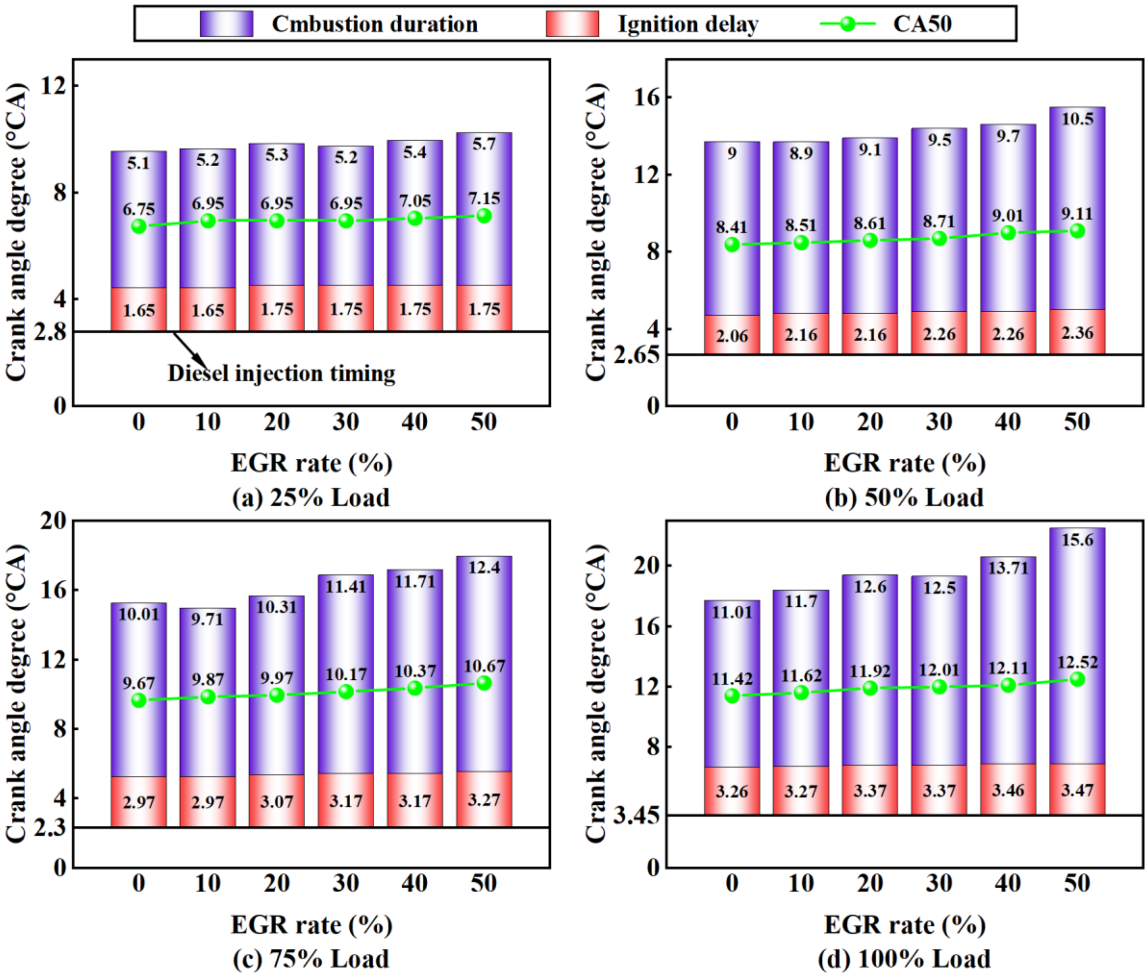

Fig. 13 Combustion phase under different loads and EGR rates

4.2 Analysis of engine work performance

The influence of EGR on energy distribution and the $IMEP_g$ under different loads is illustrated in Figure 14. It can be observed that $IMEP_g$ and ITE rise steadily with the increase of EGR rate under medium and low loads, while heat loss shows an opposite downward trend. At high loads, $IMEP_g$ and ITE increase first and then decrease as EGR rate grows, and heat loss presents a reverse trend of initial decline followed by rise. This results from the combined variation of piston work capacity and combustion state.

Figure 15 displays the variations in engine piston work under different loads. Compression work declines steadily with rising EGR across all loads, while the expansion work shows varying changes across loads due to the influence of compensatory work during the expansion process [38]. At medium and low loads, the reduced loss of expansion work, combined with the compensatory work effect, enhances the piston's work-done capability as the EGR rate increases. At high loads, the piston's work-done capability continues to improve at lower EGR rates. However, when the EGR rate goes beyond a certain threshold, the piston's work-done capability gradually weakens due to increased expansion work losses caused by the prolonged combustion duration. Compared to the 30 % EGR rate threshold at 75 % load, the threshold at 100 % load shifts earlier to 10 %, indicating that lower EGR rates should be adopted as the load increases to avoid an excessive decline in piston work-done capability.

Furthermore, it can be seen that unburned losses exhibit an increasing trend with increasing EGR rates across all loads. Since the unburned losses are minimal at the 25 % load condition, the influence of EGR is negligible. Additionally, comparing the growth magnitude of unburned losses at a 50 % EGR rate, the values for the four loads are 0, 0.02 %, 0.04 %, and 0.1 %, respectively. This indicates that unburned losses at high loads are more significantly affected by EGR. This is attributed to the long quenching distance of ammonia combustion; as the load increases, the higher ammonia content leads to deteriorated combustion at the periphery of the combustion chamber, thereby increasing the unburned ammonia content.

In summary, EGR can effectively regulate in-cylinder combustion temperature under medium and low loads, cut heat dissipation loss and improve piston work capacity. Combustion deterioration and unburned loss rise slightly in such operating conditions. The combined positive effects lead to continuous growth of ITE and $IMEP_g$ as EGR rate increases. Under high loads, large fuel injection quantity and intense initial combustion make EGR exert an inhibitory rather than promotive effect on combustion. Piston work capacity rises first and then falls. Combined with the continuous growth of unburned loss, ITE and $IMEP_g$ increase initially and decrease subsequently with rising EGR rate.

It should be noted that this study fails to separately quantify exhaust heat loss and wall heat loss when analyzing EGR effects on power performance of ammonia-fueled engines. The individual influence mechanism of EGR and load conditions on the two types of heat losses cannot be clarified independently. This limitation needs to be optimized in further research.

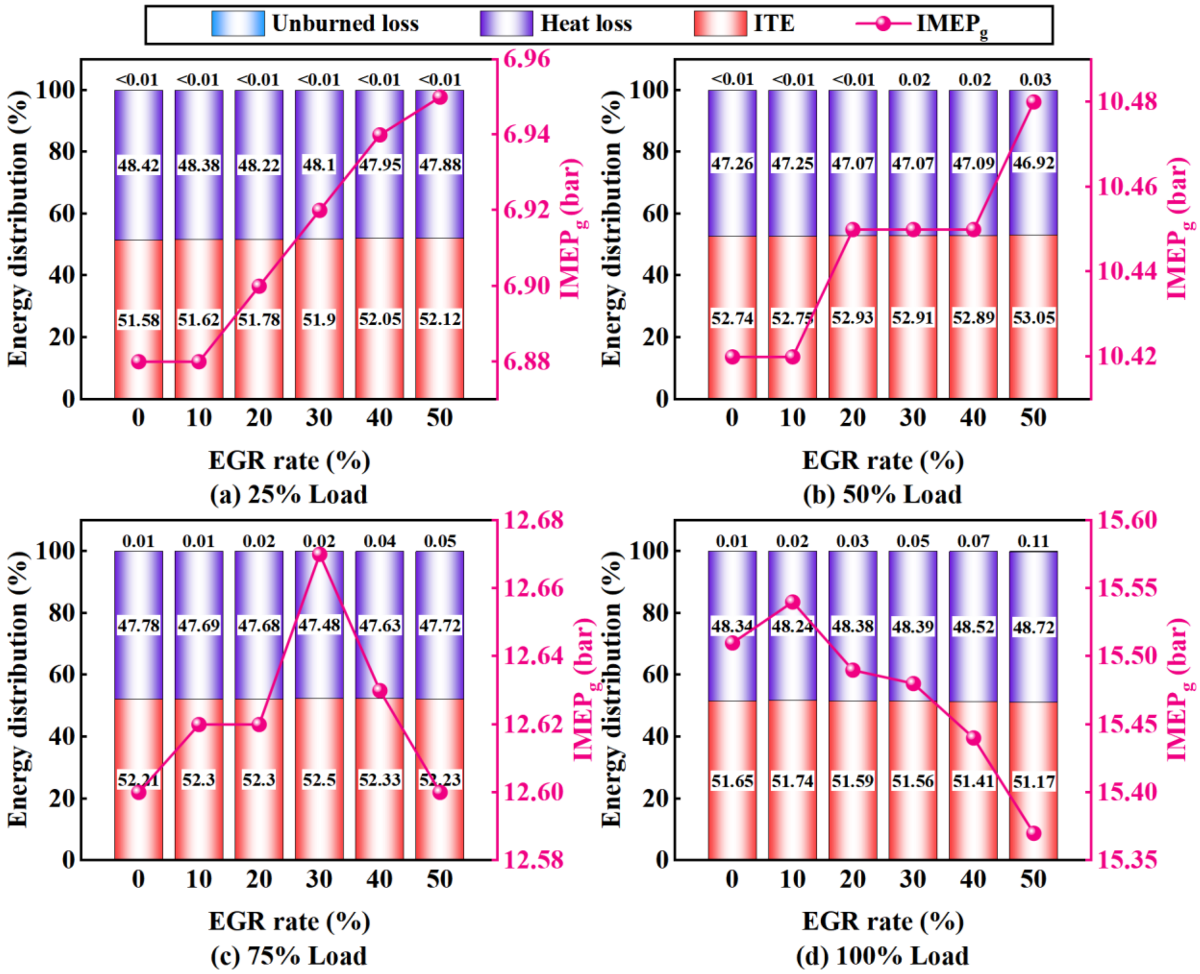

Fig. 14 Energy distribution and $IMEP_g$ under different loads and EGR rates

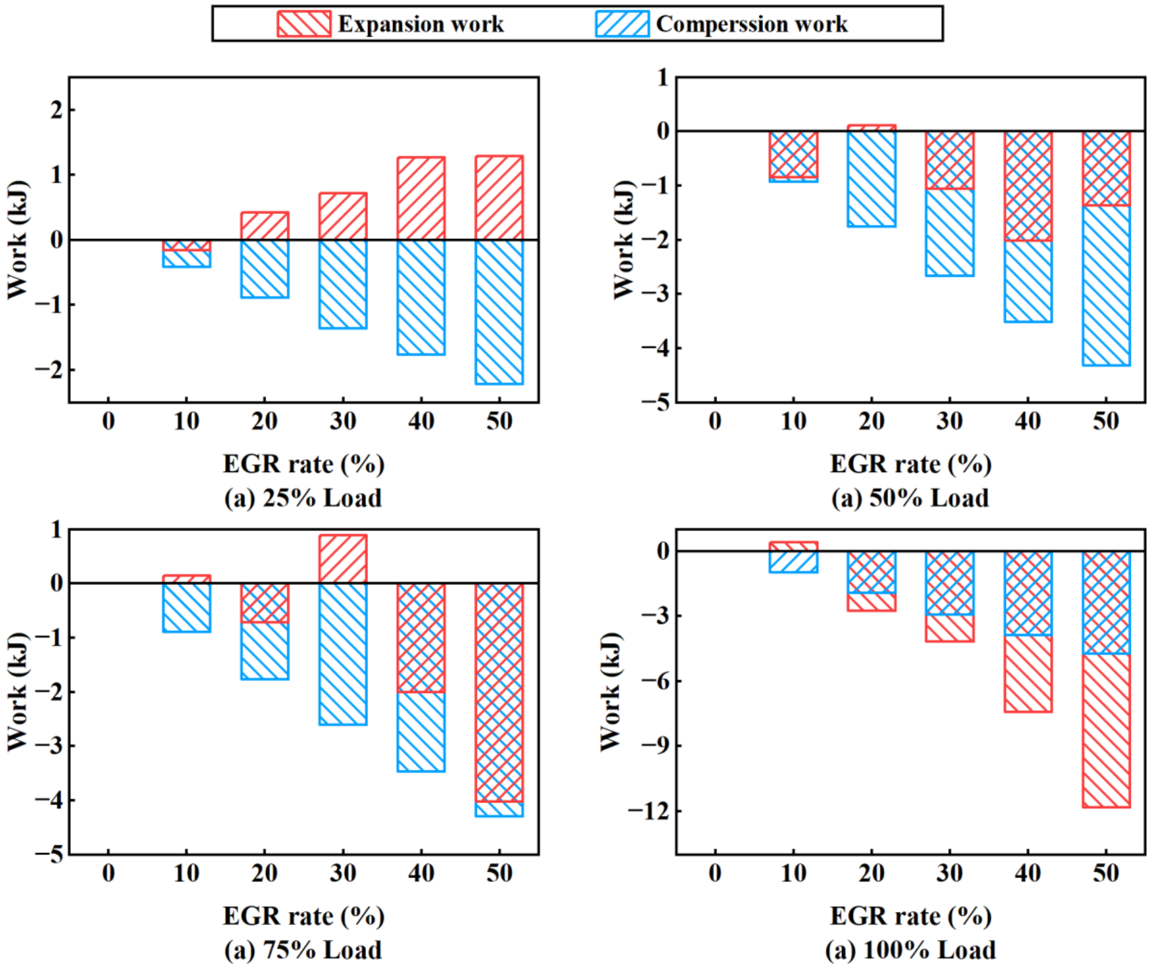

Fig. 15 Engine power output changes under different loads

4.3 Analysis of engine emission characteristics

NO_X emission is a crucial indicator for evaluating the emission performance of marine engines. In ADDF engines, due to the nitrogenous nature of the fuel, the generated NO_X can be categorized into "fuel NO_X" and "thermal NO_X". Specifically, fuel NO_X is primarily produced through the dehydrogenation and oxidation reactions of ammonia during combustion; its reaction path is illustrated in Figure 16 [41]. NH_3 generates radicals via dehydrogenation; when the temperature exceeds 1400 K, NO is produced through reactions 3-5. Thermal NO_X is mainly formed by the oxidation of N_2 in high-temperature environments (typically above 1800 K) through reactions 6-8 [42]. The formation of N_2O primarily occurs via NH_i radicals in low-temperature environments (below 1400 K) through reactions 9-10 [43].

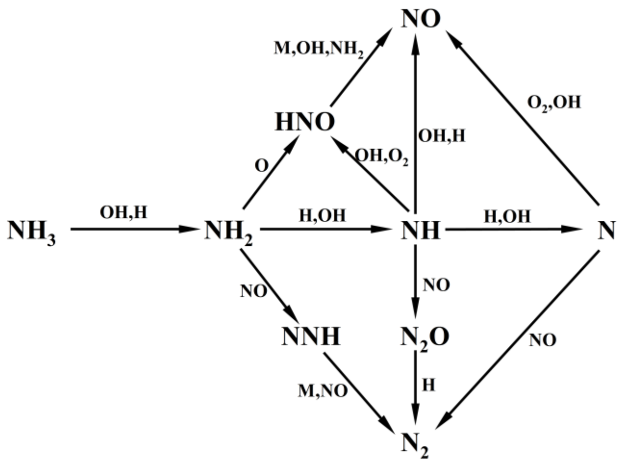

Fig. 16 Schematic diagram of the main oxidation pathways of NH_3

$$O_2 + NH_2 = H_2O + NO \tag{3}$$
$$O_2 + NH = OH + NO \tag{4}$$
$$O + NH = H + NO \tag{5}$$
$$O + N_2 = N + NO \tag{6}$$
$$O_2 + N = O + NO \tag{7}$$
$$OH + N = H + NO \tag{8}$$
$$NO + NH = H + N_2O \tag{9}$$
$$NO_2 + NH_2 = H_20 + N_2O \tag{10}$$

Figure 17 illustrates the variations in NO_X emissions under diverse load levels and EGR rates. As the EGR rate increases, NO_X emissions decrease across all loads. Firstly, the recirculated exhaust gas, with its high specific heat capacity, absorbs in-cylinder heat and reduces the cylinder temperature. Secondly, it decreases the oxygen concentration in the cylinder, which in turn slows down the combustion rate. As shown in Figure 12, the combined effect of these two factors effectively lowers the peak in-cylinder combustion temperature, the high-temperature region, and the duration of high temperatures, thereby reducing the formation of thermal NO_X. From the perspective of complying with IMO Tier III emission standards, the necessary EGR rates corresponding to 25 %, 50 %, 75 %, and 100 % load conditions are roughly 50 %, 33 %, 20 %, and 2 %, respectively. This indicates that only a very low EGR rate is required to achieve compliance at high loads, which will help reduce the application cost and difficulty of EGR on large-scale engines.

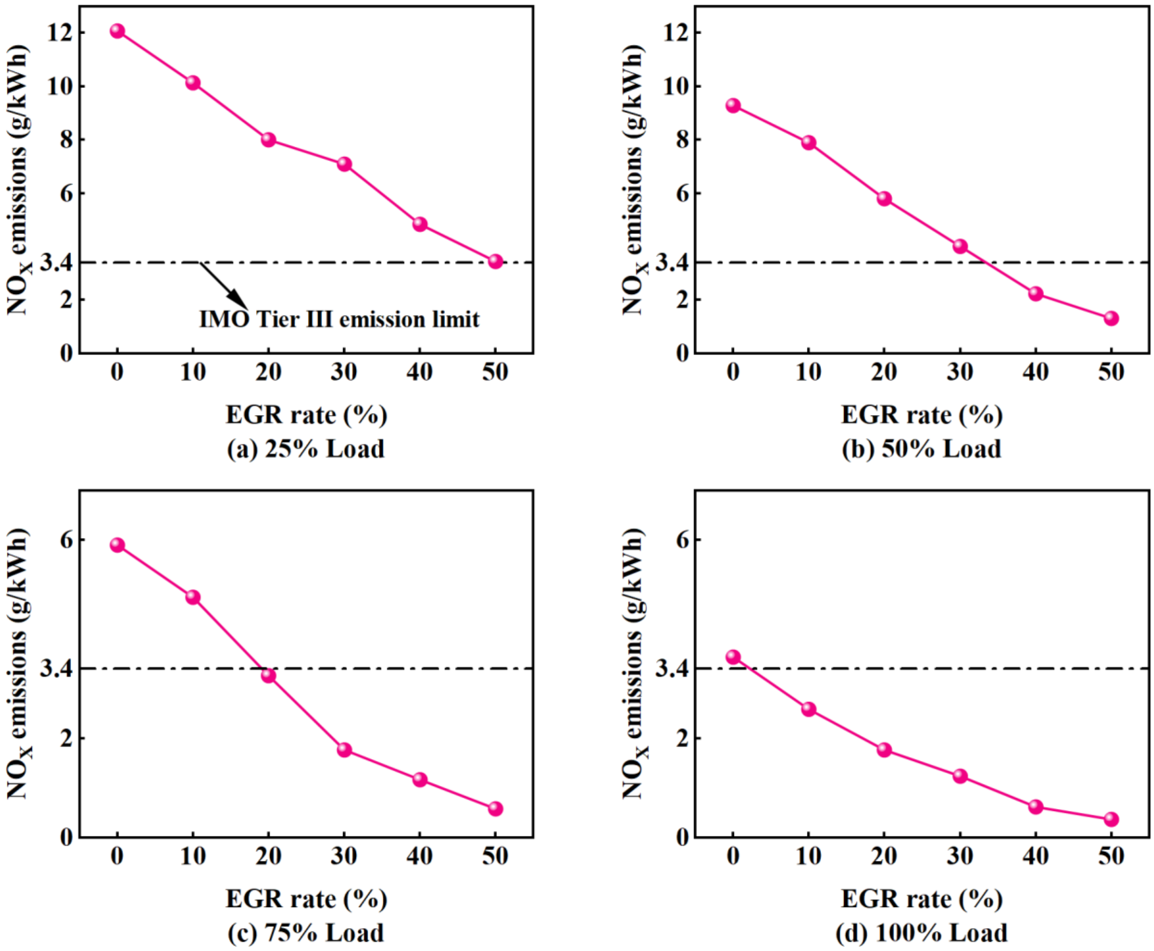

Fig. 17 NO_X emissions under different loads and EGR rates

To analyze the influence of EGR on fuel NO_X and thermal NO_X, the distribution of NO_X formation with respect to the in-cylinder equivalence ratio and temperature at 10° CA under different EGR rates is presented in Figure 18, using the 75 % load case as an example. Fuel NO_X mainly exists in regions with high equivalence ratio ($\varphi > 1$) and temperature below 1800 K, while thermal NO_X distributes in areas with low equivalence ratio ($\varphi < 1$) and temperature above 1800 K. It can be clearly observed that NO_X formation exhibits an overall decreasing trend with the increase of the EGR rate, a finding that is consistent with the pattern presented in Figure 17. A closer analysis of the patterns in the figure reveals that fuel NO_X is clearly observable only in the high equivalence ratio region under the baseline condition. When the EGR rate exceeds 10 %, the formation of fuel NO_X drops to a very low level and remains virtually unchanged. This indicates that fuel NO_X is highly sensitive to EGR, and even a low EGR rate can significantly reduce the formation of fuel NO_X. In contrast, thermal NO_X gradually decreases as the EGR rate increases; when the EGR rate reaches 50 %, substantial formation in the high-temperature region becomes difficult. This is because, as the EGR rate increases, thermal NO_X formation in the low equivalence ratio region is restricted by the drop in temperature. Reactions 6-8 are suppressed in the lower-temperature environment, leading to a reduction in thermal NO_X. In summary, it can be seen that the inhibitory effect of EGR on thermal NO_X is weaker than that on fuel NO_X; therefore, a sufficiently high EGR rate is required to effectively mitigate NO_X emissions.

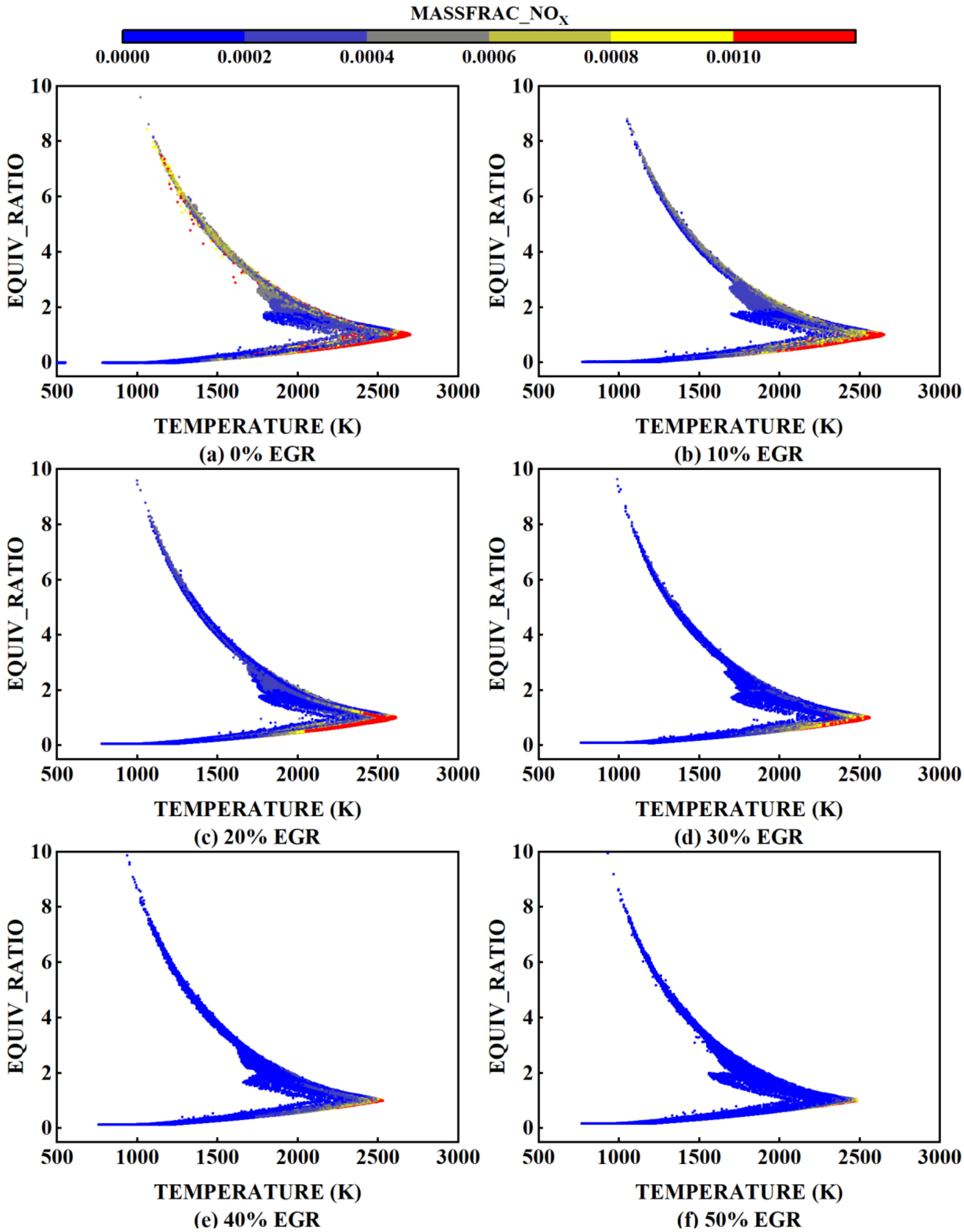

Fig. 18 Equivalence ratio-temperature distribution at 75 % load and 10 °CA ATDC

Figure 19 presents the unburned ammonia emissions and N_2O under various loads and EGR rates. Generally, unburned ammonia emissions exhibit an increasing trend with the increase of the EGR rate across all loads. Since the amount of unburned ammonia at 25 % load is very low, the impact of EGR is negligible. It is worth noting that when the EGR rate exceeds a certain range, the unburned ammonia emissions increase significantly. For loads from 50 % to 100 %, the corresponding EGR rates are 30 %, 40 %, and 50 %, with corresponding growth rates of 356 %, 161 %, and 64 %, respectively. This result indicates that compared to medium loads, the unburned ammonia growth rate under high load conditions exhibits a higher tolerance to EGR.

Figure 20 illustrates the in-cylinder distribution of unburned ammonia at the moment of exhaust valve opening under different loads and EGR rates. It can be observed that under all loads, unburned ammonia primarily accumulates at the bottom of the combustion chamber and in the piston ring area. This is the result of the combined effect of the inherently slow flame propagation speed of ammonia and the decrease in temperature and oxygen concentration caused by the introduction of EGR. The low-temperature and low-oxygen environment leads to a reduction in the flame area; consequently, the ammonia located at the bottom of the combustion chamber and in the piston crevices cannot be swept by the flame, resulting in the accumulation of unburned ammonia. As the EGR rate increases, the reduction in temperature and high-temperature regions (as shown in Figure 12) further promotes the expansion of the unburned ammonia accumulation area, leading to the phenomenon of increased unburned ammonia emissions.

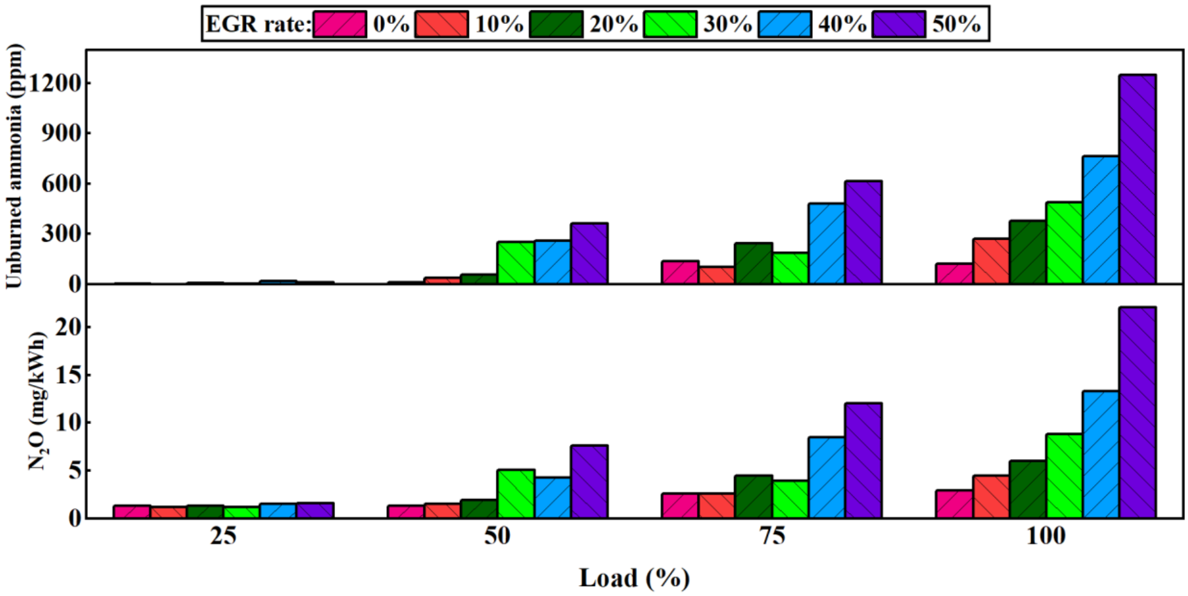

Fig. 19 Unburned ammonia and N_2O emissions under different loads and EGR rates

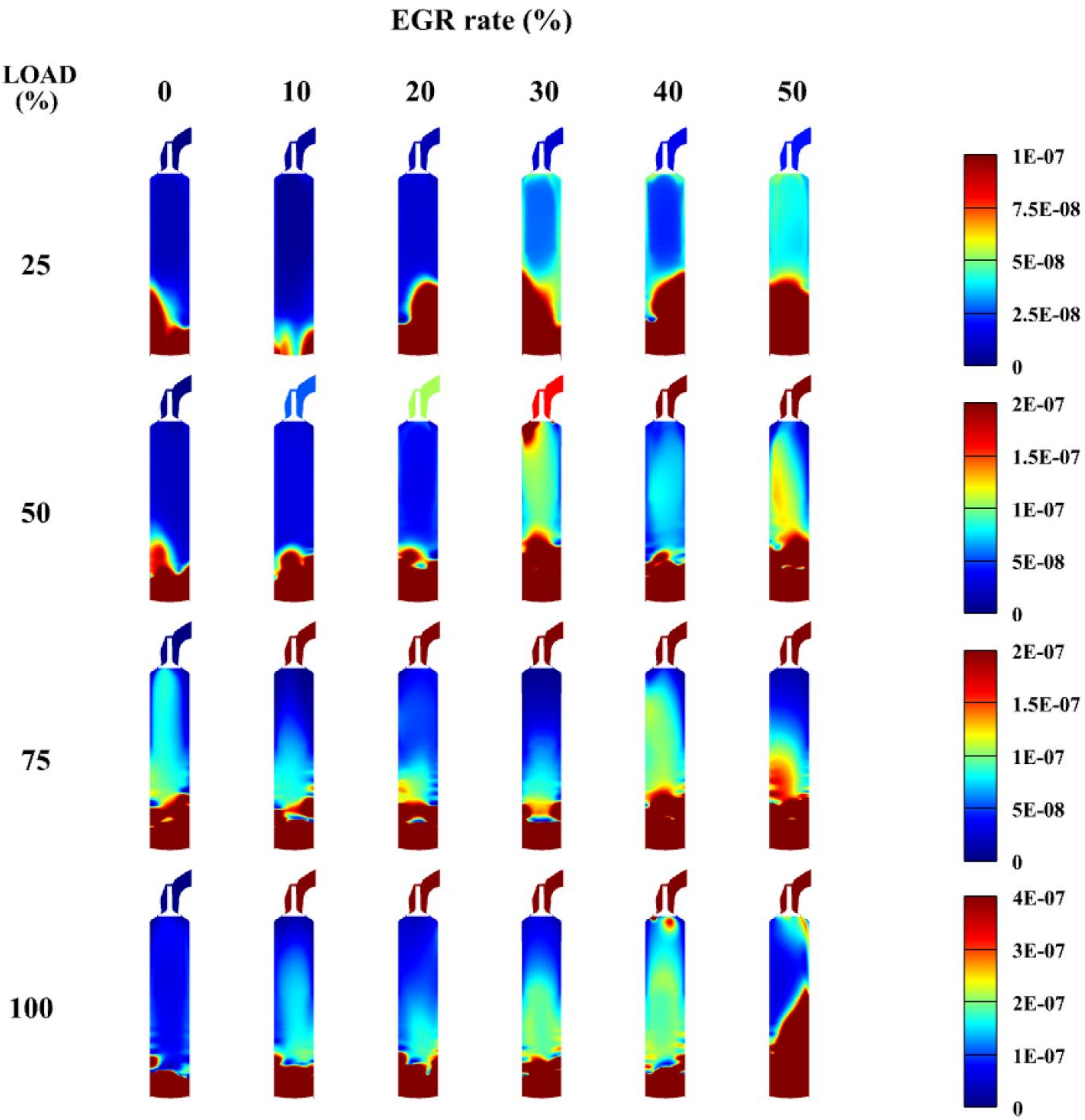

Fig. 20 Distribution of unburned ammonia in the cylinder at different loads and EGR rates at the moment of exhaust valve opening

Research indicates that the greenhouse effect of N_2O is 298 times that of CO_2 [44]; therefore, N_2O is a greenhouse gas of significant concern. Observe the impact of EGR on N_2O emissions under diverse loads in Figure 19, it can be found that at low load (25 % load), EGR has a minor impact on N_2O emissions. From 50 % load to 100 % load, N_2O emissions generally exhibit an upward trend as the EGR rate increases. Figure 21 displays the variations in in-cylinder N_2O and NH_i radical content at 100 % load. It can be observed that the in-cylinder N_2O content does not generally increase with the introduction of EGR during the ammonia combustion phase (the angle interval corresponding to the red box in Figure 11), whereas it increases continuously with the EGR rate during the post-combustion phase (the angle interval corresponding to the green box in Figure 11). This indicates that, compared to the baseline condition, the increased N_2O in the exhaust emissions under EGR conditions originates primarily from the post-combustion phase. The primary reason is that high EGR conditions generate more NH_i radicals during the ammonia combustion phase, thereby promoting the progression of reactions 9-10, which ultimately results in increased N_2O emissions.

Carefully observe Figure 19, it can also be found that the engine's unburned ammonia and N_2O emissions exhibit similar trends under various loads and EGR rates. Under low load, the introduction of EGR does not significantly affect unburned ammonia and N_2O emissions; however, under medium and high loads, both unburned ammonia and N_2O emissions rise significantly as the EGR rate increases. This suggests that EGR exerts the same influence pattern on both unburned ammonia and N_2O emissions from the engine.

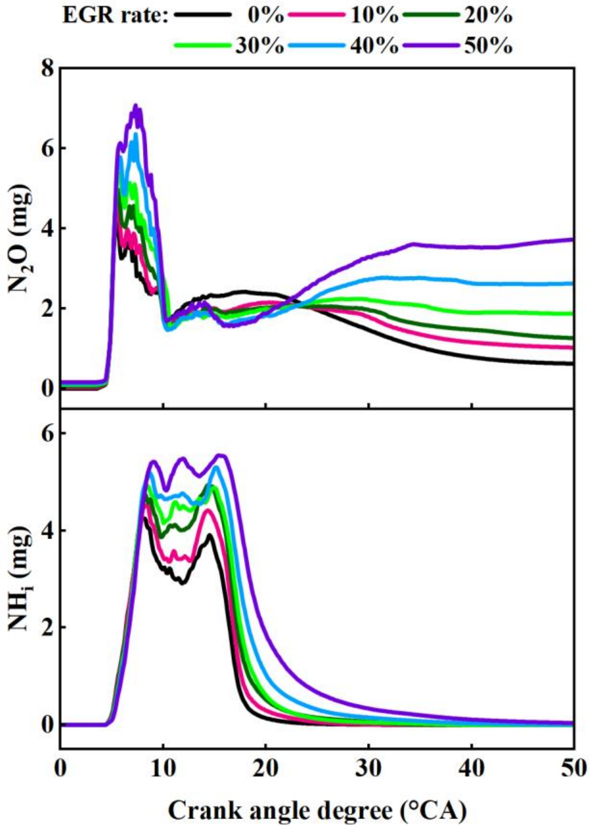

Fig. 21 Changes in N_2O and NH_i radical content in the cylinder at 100 % load

4.4 Recommendation for EGR optimization strategy

Comprehensively considering the influence of EGR on engine work performance and emissions, a full-load-range EGR optimization strategy is proposed. The advised EGR rates for 25 %, 50 %, 75 %, and 100 % load levels are around 50 %, 40 %, 30 %, and 10 %, respectively. The $IMEP_g$, NO_X, and N_2O emissions corresponding to these optimization points are shown in Fig. 22. The reasons for recommending this scheme are as follows:

- The NO_X emissions corresponding to the four loads are 3.4, 2.2, 1.8, and 2.6 g/kWh, representing reductions of 71.5 %, 75.9 %, 70.0 %, and 28.8 % compared to the baseline conditions, respectively. Both the individual load and weighted NO_X emissions comply with the IMO Tier III regulations and possess a sufficient margin.
- N_2O and ammonia emissions are maintained at low levels to avoid increasing toxic gas emissions and the greenhouse effect. It should be noted that the analysis results in Section 4.3 indicate that ammonia and N_2O emissions share the same trend; therefore, N_2O emissions are used to represent the ammonia emission trend in Figure 22. This allows the optimization parameters to be reduced from four to three, thereby more clearly demonstrating the trade-offs among multiple variables.
- Engine work performance is improved. The $IMEP_g$ values corresponding to the four loads are 6.95, 10.45, 12.67, and 15.54 bar, representing increases of 1.04 %, 0.58 %, 0.56 %, and 0.18 % compared to the baseline conditions, respectively.

- The EGR rate configuration principle is suitable for the application scenarios of the studied engine. Large marine two-stroke engines have high exhaust gas flow rates, which increase with load. Therefore, applying EGR technology requires a rational design of the EGR scheme to minimize the rated capacity of the EGR system, thereby reducing the operating costs of the EGR system and the engine room space occupied [22]. In the recommended scheme, the EGR rate gradually decreases as the load increases, reaching only 10 % at 100 % load, which will effectively reduce the rated capacity of the EGR system.

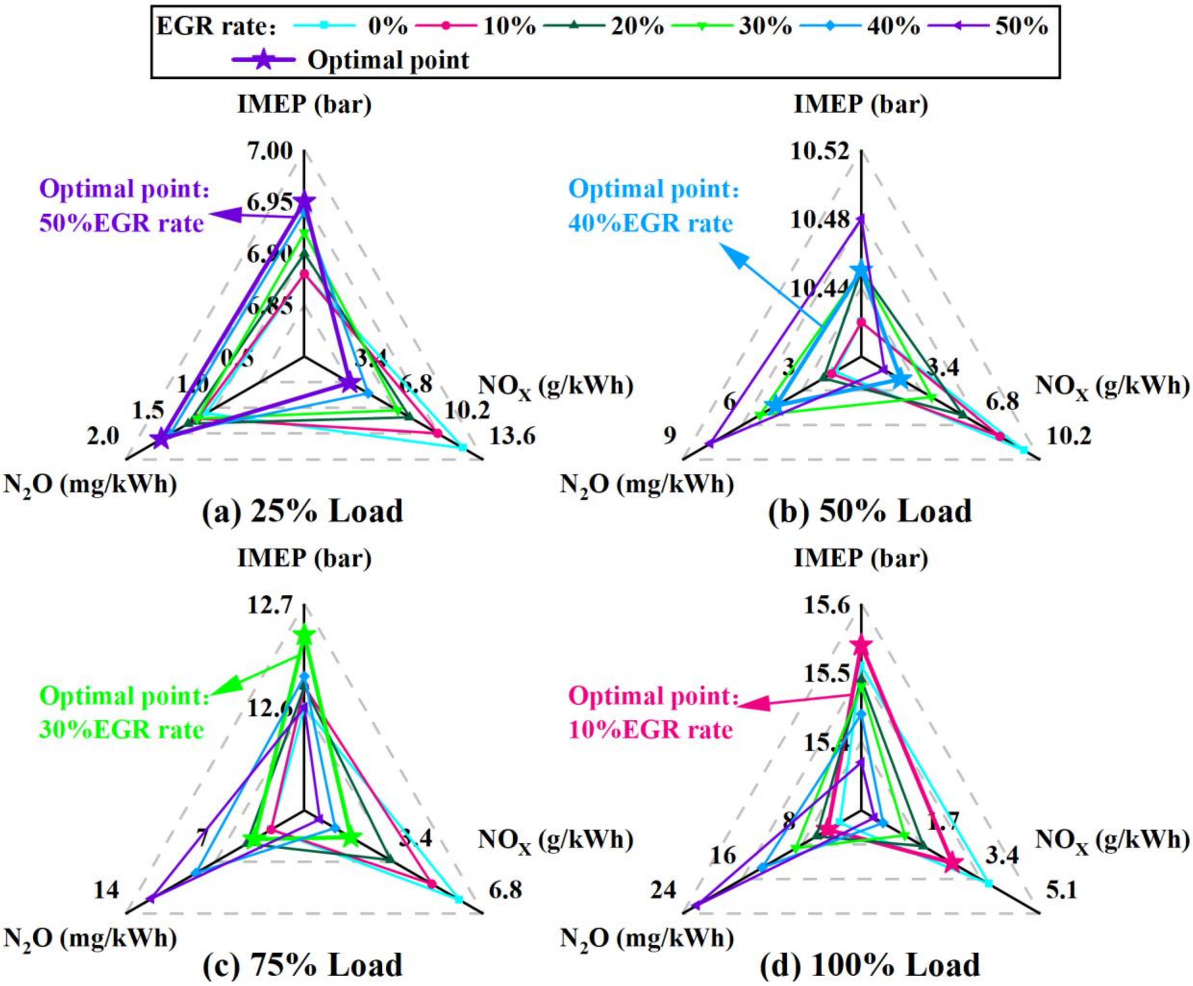

Fig. 22 Distribution of comprehensive evaluation points

5. Conclusions

In this study, a 3D CFD simulation model of a marine two-stroke high-pressure direct-injection ADDF engine was established. Based on this, this work systematically reveals for the first time the effects of EGR rates ranging from 0 % to 50 % on the combustion, performance, and emission characteristics of the engine under the dual-fuel combustion mode at four loads: 25 %, 50 %, 75 %, and 100 %. The core conclusions of this study can be summarized as follows:

- Under all investigated load conditions, increasing the EGR rate reduces the compression pressure and peak in-cylinder pressure, prolongs the ignition delay and combustion duration, and continuously increases unburned ammonia losses. Such effects are more pronounced at high engine loads.
- At low and medium loads, the $IMEP_g$ increases with a rising EGR rate. By contrast, a critical EGR threshold exists at high loads, which advances gradually as the load increases. Therefore, a low EGR rate is required to avoid engine performance deterioration.

- EGR effectively reduces NO_X emissions across all operating loads. When the EGR rate reaches 50 %, the NO_X emission reduction range is up to 71.5-90.2 %. Fuel NO_X is highly sensitive to EGR, and a slight increase in the EGR rate can significantly suppress its formation. In comparison, thermal NO_X is less affected by EGR, and a higher EGR rate is required to achieve effective control of thermal NO_X generation.
- At low loads, the application of EGR exerts a negligible influence on unburned ammonia and N_2O emissions. Nevertheless, at medium and high loads, both ammonia and N_2O emissions rise significantly with increasing EGR rates, exhibiting an obvious threshold characteristic. Strict EGR rate regulation is essential to balance NO_X reduction and the control of ammonia and N_2O emissions.
- Comprehensively considering engine performance and emission characteristics, the recommended EGR rates at 25 %, 50 %, 75 %, and 100 % load levels are 50 %, 40 %, 30 %, and 10 %, respectively. This strategy allows for a significant reduction in NO_X emissions compared to baseline conditions at each load, maintains NH_3 and N_2O emissions at low levels, and increases $IMEP_g$ to varying degrees relative to the baseline.

In summary, employing an appropriate EGR strategy in two-stroke high-pressure direct injection ADDF engines can achieve simultaneous improvements in performance and emissions while complying with IMO Tier III regulations. However, the EGR strategy must be adjusted according to the combustion and emission characteristics of different loads to avoid engine performance deterioration. Additionally, the increase in unburned ammonia and N_2O emissions caused by EGR should not be overlooked. Future research will focus on the synergistic optimization of ADDF injection strategies and EGR to further improve engine combustion and emissions.

ACKNOWLEDGMENTS

The authors greatly acknowledge Everllence and CSSC Engine Co., Ltd for providing technical support for engine simulation modeling and validation.

FUNDING

This word was supported by the Liaoning Provincial Science and Technology Plan Joint Program (Natural Science Foundation) [Grant No. 2025-BSLH-052]; the National Key R&D Program of China [grant number 2022YFB4301400].

ABBREVIATIONS

ADDF	Ammonia/diesel dual-fuel
ATDC	After top dead center
CA	Crank angle
CA10	Crank angle corresponding to 10 % of total heat release
CA50	Crank angle corresponding to 50 % of total heat release
CA90	Crank angle corresponding to 90 % of total heat release
CFD	Computational fluid dynamics
EGR	Exhaust gas recirculation
GHG	Greenhouse gas
HPDI	High-pressure liquid ammonia direct injection combustion
HRR	Heat release rate
$IMEP_g$	Gross indicated mean effective pressure
IMO	International Maritime Organization

ITE Indicated thermal efficiency
LHV Lower heating value
LPGI Low-pressure ammonia gas injection premixed combustion
NO_X Nitrogen oxides
N_2O Nitrous oxide
W_{gross} The gross work done by the piston
3D Three dimensional

APPENDIX A

Table A.1 Gas component settings for research cases

Load	**EGR rate**	**Mass fraction**					
[%]	**[%]**	**O_2**	**N_2**	**CO_2**	**H_2O**	**NH_3**	**N_2O**
25	0	0.233	0.767	-	-	-	-
	10	0.224972843	0.766900257	0.001701584	0.006425295	0.000000004	0.000000017
	20	0.216945686	0.766800516	0.003403168	0.012850589	0.000000008	0.000000033
	30	0.208918529	0.766700774	0.005104751	0.019275884	0.000000012	0.00000005
	40	0.200891372	0.76660103	0.006806335	0.025701179	0.000000017	0.000000067
	50	0.192864215	0.766501289	0.008507919	0.032126473	0.000000021	0.000000083
50	0	0.233	0.767	-	-	-	-
	10	0.22252831	0.767045951	0.00148176	0.008943902	0.000000054	0.000000023
	20	0.21205662	0.767091902	0.002963521	0.017887804	0.000000107	0.000000046
	30	0.20158493	0.767137852	0.004445281	0.026831706	0.000000161	0.00000007
	40	0.191113239	0.767183804	0.005927042	0.035775607	0.000000215	0.000000093
	50	0.180641549	0.767229755	0.007408802	0.044719509	0.000000269	0.000000116
75	0	0.233	0.767	-	-	-	-
	10	0.223836725	0.767132247	0.000877495	0.008152829	0.000000665	0.000000039
	20	0.214673449	0.767264495	0.001754991	0.016305658	0.00000133	0.000000077
	30	0.205510174	0.767396742	0.002632486	0.024458487	0.000001995	0.000000116
	40	0.196346899	0.76752899	0.003509981	0.032611316	0.00000266	0.000000154
	50	0.187183623	0.767661237	0.004387476	0.040764145	0.000003326	0.000000193

100	0	0.233	0.767	-	-	-	-
	10	0.223590561	0.76720809	0.000588561	0.008612116	0.000000628	0.000000044
	20	0.214181122	0.767416182	0.001177121	0.017224231	0.000001256	0.000000088
	30	0.204771683	0.767624272	0.001765682	0.025836347	0.000001884	0.000000132
	40	0.195362244	0.767832363	0.002354243	0.034448462	0.000002512	0.000000176
	50	0.185952805	0.768040453	0.002942804	0.043060578	0.00000314	0.00000022

REFERENCES

[1] Zhang, J., Wang, S., Wang, Z., Xie, Z., Chang, Y., 2025. Investigation of intake and exhaust performance in heavy-duty diesel engines with variable Miller cycle. *Applied Thermal Engineering*, 265, 125547. https://doi.org/10.1016/j.applthermaleng.2025.125547

[2] Prados, J. M. M., Fernandez, I. A., Gomez, M. R., Parga, M. N., 2024. The decarbonisation of the maritime sector: Horizon 2050. *Brodogradnja*, 75(2), 75202. https://doi.org/10.21278/brod75202

[3] Chen, G., Wei, F., Zhang, K., Xiao, R., Wang, Z., Yang, S., 2023. Investigation on combustion characteristics and gas emissions of a high-pressure direct-injection natural gas engine at different combustion modes. *Energy Conversion and Management*, 277, 116617. https://doi.org/10.1016/j.enconman.2022.116617

[4] Tuswan, T., Sari, D. P., Muttaqie, T., Prabowo, A. R., Soetardjo, M., Murwantono, et al., 2023. Representative application of LNG-fuelled ships: a critical overview on potential GHG emission reductions and economic benefits. *Brodogradnja*, 74(1), 63-83. https://doi.org/10.21278/brod74104

[5] Jayabal, R., 2024. Ammonia as a potential green dual fuel in diesel engines: A review. *Process Safety and Environmental Protection*, 188, 1346-1354. https://doi.org/10.1016/j.psep.2024.06.012

[6] Qi, Y., Liu, W., Liu, S., Wang, W., Peng, Y., Wang, Z., 2023. A review on ammonia-hydrogen fueled internal combustion engines. *ETransportation*, 18, 100288. https://doi.org/10.1016/j.etran.2023.100288

[7] Huang, Y., Lyu, L., Yang, H., Liang, J., Chen, Y., Chen, Q., Zhu, N., 2025. Effects of diesel injection method and timing on combustion and emission characteristics of marine ammonia/diesel dual-fuel engine. *Applied Thermal Engineering*, 278, 127266. https://doi.org/10.1016/j.applthermaleng.2025.127266

[8] Rocha, R. C., Zhong, S., Xu, L., Bai, X.-S., Costa, M., Cai, X., et al., 2021. Structure and laminar flame speed of an ammonia/methane/air premixed flame under varying pressure and equivalence ratio. *Energy & Fuels*, 35(9), 7179-7192. https://doi.org/10.1021/acs.energyfuels.0c03520

[9] Nguyen, X. P., Bora, B. J., Olcer, A. I., Sharma, P., Nguyen, V. N., Cao, D. N., 2025. Effect of compression ratio on dual-fuel diesel engine fueled with ammonia: Experimental and statistical analysis. *Process Safety and Environmental Protection*, 195, 106810. https://doi.org/10.1016/j.psep.2025.106810

[10] Zhou, X., Li, T., Wang, N., Wang, X., Chen, R., Li, S., 2023. Pilot diesel-ignited ammonia dual fuel low-speed marine engines: A comparative analysis of ammonia premixed and high-pressure spray combustion modes with CFD simulation. *Renewable and Sustainable Energy Reviews*, 173, 113108. https://doi.org/10.1016/j.rser.2022.113108

[11] Reiter, A. J., Kong, S.-C., 2010. Diesel engine operation using ammonia as a carbon-free fuel. *Fall Technical Conference of the ASME Internal Combustion Engine Division*, 12-15 September, SW Res Inst, San Antonio, Texas, USA. https://doi.org/10.1115/ICEF2010-35026

[12] Zhu, J., Zhou, D., Yang, W., Qian, Y., Mao, Y., Lu, X., 2023. Investigation on the potential of using carbon-free ammonia in large two-stroke marine engines by dual-fuel combustion strategy. *Energy*, 263, 125748. https://doi.org/10.1016/j.energy.2022.125748

[13] Liu, L., Wu, Z., Tan, F., Wang, Y., 2023. CFD investigation the combustion characteristic of ammonia in low-speed marine engine under different combustion modes. *Fuel*, 351, 128906. https://doi.org/10.1016/j.fuel.2023.128906

[14] Zhang, Z., Long, W., Dong, P., Tian, H., Tian, J., Li, B., Wang, Y., 2023. Performance characteristics of a two-stroke low speed engine applying ammonia/diesel dual direct injection strategy. *Fuel*, 332, 126086. https://doi.org/10.1016/j.fuel.2022.126086

[15] Liu, H., Lu, D., Shen, H., Chang, L., Gan, H., 2026. Numerical investigation on performance optimization and GHG emissions reduction of marine two-stroke natural gas dual-fuel engines. *Applied Thermal Engineering*, 289, 129867. https://doi.org/10.1016/j.applthermaleng.2026.129867

[16] Xiong, Q., Han, K., Shi, X., Pan, C., Liu, L., 2026. Numerical study on injection strategy of marine low-speed engines under high pressure direct injection ammonia/diesel dual fuel mode. *Energy*, 350, 140709. https://doi.org/10.1016/j.energy.2026.140709

[17] Chen, D., Zhang, J., Yang, C., Sun, B., Wang, T., Wang, Y., 2026. Effects of critical parameters on combustion and emission characteristics of large-scale marine two-stroke HPDI diesel/methanol dual-fuel engine under different conditions. *Applied Thermal Engineering*, 298, 130969. https://doi.org/10.1016/j.applthermaleng.2026.130969

[18] Ma, B., Liu, B., Wang, Y., Liu, L., 2025. Analysis on the combustion performance of ammonia-hydrogen coaxial stratified injection in low speed marine engine. *Applied Thermal Engineering*, 270, 126253. https://doi.org/10.1016/j.applthermaleng.2025.126253

[19] Chai, W. S., Bao, Y., Jin, P., Tang, G., Zhou, L., 2021. A review on ammonia, ammonia-hydrogen and ammonia-methane fuels. *Renewable and Sustainable Energy Reviews*, 147, 111254. https://doi.org/10.1016/j.rser.2021.111254

[20] Yao, N., Pan, W., Zhang, J., Wei, L., 2024. The advancement on carbon-free ammonia fuels for gas turbine: A review. *Energy Conversion and Management*, 315, 118745. https://doi.org/10.1016/j.enconman.2024.118745

[21] Otomo, J., Koshi, M., Mitsumori, T., Iwasaki, H., Yamada, K., 2018. Chemical kinetic modeling of ammonia oxidation with improved reaction mechanism for ammonia/air and ammonia/hydrogen/air combustion. *International Journal of Hydrogen Energy*, 43(5), 3004-3014. https://doi.org/10.1016/j.ijhydene.2017.12.066

[22] Tang, X., Wang, P., Zhang, Z., Zhang, F., Shi, L., Deng, K., 2022. Effects of high-pressure and donor-cylinder exhaust gas recirculation on fuel economy and emissions of marine diesel engines. *Fuel*, 309, 122226. https://doi.org/10.1016/j.fuel.2021.122226

[23] Lu, D., Theotokatos, G., Zhang, J., Zeng, H., Cui, K., 2022. Parametric investigation of a large marine two-stroke diesel engine equipped with exhaust gas recirculation and turbocharger cut out systems. *Applied thermal engineering*, 200, 117654. https://doi.org/10.1016/j.applthermaleng.2021.117654

[24] Abd-Alla, G. H., 2002. Using exhaust gas recirculation in internal combustion engines: a review. *energy conversion and management*, 43(8), 1027-1042. https://doi.org/10.1016/S0196-8904(01)00091-7

[25] Sun, W., Wang, X., Guo, L., Zhang, H., Zeng, W., Lin, S., et al., 2025. Study on effects of EGR and injection strategies on the combustion and emission characteristics of ammonia/diesel dual-fuel engine. *Energy*, 315, 134391. https://doi.org/10.1016/j.energy.2025.134391

[26] Li, T., Zhou, X., Wang, N., Wang, X., Chen, R., Li, S., Yi, P., 2022. A comparison between low-and high-pressure injection dual-fuel modes of diesel-pilot-ignition ammonia combustion engines. *Journal of the Energy Institute*, 102, 362-373. https://doi.org/10.1016/j.joei.2022.04.009

[27] Lu, D., Wang, A., Gan, H., Su, Y., Ao, X., 2025. A multi-objective collaborative optimization method of ship energy efficiency based on NSGA-II and TOPSIS. *Brodogradnja*, 76(3), 76301. https://doi.org/10.21278/brod76301

[28] Han, Z., Reitz, R. D., 1995. Turbulence modeling of internal combustion engines using RNG κ-ε models. *Combustion science and technology*, 106(4-6), 267-295. https://doi.org/10.1080/00102209508907782

[29] Beale, J. C., Reitz, R. D., 1999. Modeling spray atomization with the Kelvin-Helmholtz/Rayleigh-Taylor hybrid model. *Atomization and sprays*, 9(6), 623-650. https://doi.org/10.1615/AtomizSpr.v9.i6.40

[30] Reitz, R. D., Diwakar, R., 1987. Structure of high-pressure fuel sprays. *SAE transactions*, 492-509. https://doi.org/10.4271/870598

[31] Shi, C., Ji, C., Wang, S., Yang, J., Ma, Z., Ge, Y., 2019. Combined influence of hydrogen direct-injection pressure and nozzle diameter on lean combustion in a spark-ignited rotary engine. *Energy Conversion and Management*, 195, 1124-1137. https://doi.org/10.1016/j.enconman.2019.05.095

[32] Schmidt, D. P., Rutland, C. J., 2000. A new droplet collision algorithm. *Journal of Computational Physics*, 164(1), 62-80. https://doi.org/10.1006/jcph.2000.6568

[33] Shi, T., Pei, Y., Jin, S., Zi, Z., Wang, X., Zhang, F., Wu, B., 2025. Analysis of the influence of ammonia energy ratio and injection timing on the formation of ultrafine particles in an Ammonia-Diesel Dual-Fuel (ADDF) engine. *Energy*, 334, 137556. https://doi.org/10.1016/j.energy.2025.137556

[34] Liu, Y.-D., Jia, M., Xie, M.-Z., Pang, B., 2012. Enhancement on a skeletal kinetic model for primary reference fuel oxidation by using a semidecoupling methodology. *Energy & Fuels*, 26(12), 7069-7083. https://doi.org/10.1021/ef301242b

[35] Zhu, Z., Zhong, X., Zhao, X., Wang, Y., Zheng, Z., Yao, M., Wang, H., 2021. Numerical investigation on combustion system optimization of stoichiometric operation natural gas engine based on knocking boundary extension. *Fuel*, 290, 120092. https://doi.org/10.1016/j.fuel.2020.120092

[36] Liu, W., Jiang, Y., Zhang, B., Chen, Y., 2023. Numerical study on effects of EGR on combustion and NOx emissions of gasoline blended dissociated methanol gas engine. *Energy Reports*, 9, 245-249. https://doi.org/10.1016/j.egyr.2023.09.174

[37] Hiroyasu, H., Kadota, T., 1976. Models for combustion and formation of nitric oxide and soot in direct injection diesel engines. *SAE transactions*, 513-526. https://doi.org/10.4271/760129

[38] Hu, H., Lu, D., Zhang, X., Gan, H., Huang, Z., 2025. Study of EGR strategy for marine two-stroke methanol-diesel dual-fuel engines: Combustion, performance, and emission analysis across full operating range. *Thermal Science and Engineering Progress*, 66, 104058. https://doi.org/10.1016/j.tsep.2025.104058

[39] Zhou, X., Li, T., Chen, R., Wei, Y., Wang, X., Wang, N., et al., 2024. Ammonia marine engine design for enhanced efficiency and reduced greenhouse gas emissions. *Nature Communications*, 15(1), 2110. https://doi.org/10.1038/s41467-024-46452-z

[40] Nie, X., Bi, Y., Shen, L., Lei, J., Wan, M., Xiao, Y., Chen, G., 2024. Experimental study for optimizing EGR strategy in an ammonia-diesel dual-fuel engine under different altitudes. *Energy*, 313, 133953. https://doi.org/10.1016/j.energy.2024.133953

[41] Miller, J. A., Smooke, M. D., Green, R. M., Kee, R. J., 1983. Kinetic modeling of the oxidation of ammonia in flames. *Combustion Science and Technology*, 34(1-6), 149-176. https://doi.org/10.1080/00102208308923691

[42] Wang, L., Gan, H., Li, Y., Liu, Y., Lu, D., Wang, H., 2025. Numerical investigation of ammonia-diesel dual-fuel engine based on ammonia thermal cracking for hydrogen to reduce unburned ammonia and GHG. *Energy*, 336, 138523. https://doi.org/10.1016/j.energy.2025.138523

[43] Liu, L., Wu, J., Liu, H., Wu, Y., Wang, Y., 2024. Investigation of combustion and emissions characteristics in a low-speed marine engine using ammonia under thermal and reactive atmospheres. *International Journal of Hydrogen Energy*, 63, 1237-1247. https://doi.org/10.1016/j.ijhydene.2024.02.308

[44] Xu, Q.-Y., Chen, Y.-F., Yao, N.-N., Zhang, J.-K., Huang, Y., Han, D., Pan, W.-G., 2025. Recent advancements in ammonia catalytic cracking and waste heat reforming technologies: A review. *Energy Conversion and Management*, 326, 119530. https://doi.org/10.1016/j.enconman.2025.119530